Calculations of electron mobility in II-VI semiconductors

Nenad Vukmirović*
Institute of Physics Belgrade, University of Belgrade, Pregrevica 118, 11080 Belgrade, Serbia

(Received 19 March 2021; revised 31 May 2021; accepted 5 August 2021; published 19 August 2021)

Electron mobility in the conduction band of II-VI semiconductors ZnSe, CdTe, ZnTe, and CdSe was studied. Temperature dependence of mobility was calculated using the methodology based on density functional theory calculations of the electronic states, phonon modes, and electron-phonon coupling constants, along with Fourier-Wannier procedure for interpolation to a dense grid in momentum space. The mobilities obtained from calculations within generalized gradient approximation of density functional theory overestimate the experimental mobility several times. The calculation that used improved electronic band structure and high-frequency dielectric constants obtained using a hybrid functional lead to a very good agreement with experimental mobilities for most of the materials studied. It was also found that the Fröhlich model provides a reasonably good estimate of mobilities around room temperature where longitudinal optical phonons provide the dominant scattering mechanism, as expected for these direct gap materials where all relevant electronic states are in the vicinity of the Γ point. The results indicate as well that the long-ranged part of electron-phonon interaction fully determines the electron mobility in the materials studied. For this reason, the approach where only this part of electron-phonon interaction is calculated using the relevant analytical formulas allows for accurate calculation of mobility without the use of the interpolation procedure for electron-phonon coupling constants.

DOI: 10.1103/PhysRevB.104.085203

I. INTRODUCTION

Mobility of charge carriers (electrons or holes) in a semiconductor material is a physical quantity that strongly affects the performance of electronic and optoelectronic devices based on that material. While it is relatively straightforward to perform the measurement of its value, it is still challenging to theoretically predict it starting from the crystal structure of the material.

The mobility of charge carriers in ultrapure samples is limited by the interaction of charge carriers with phonons. In realistic samples at room temperature it is typically also the carrier-phonon interaction that limits the mobility, whereas at low temperatures and high impurity concentration the scattering of carriers on impurities may play the dominant role. For these reasons, it is necessary to study the electronic structure, the phonon dispersions and the interaction between electrons and phonons to obtain the mobility of charge carriers in the material.

Density functional theory (DFT) [1–3] and density functional perturbation theory (DFPT) [4,5] give a theoretical framework for calculation of electronic states, phonon modes, and electron-phonon coupling constants. However, several challenges had to be overcome to come to a practical scheme that can be used to evaluate phonon-limited electron mobility of a semiconducting material. The electron-phonon coupling constants can vary rapidly as a function of phonon or electron momentum and for this reason a dense momentum grid in the first Brillouin zone is required to accurately represent them and to reliably calculate the physical quantities that depend on them. On the other hand, reliable electronic structure and phonon dispersions can be obtained from the calculations on a relatively coarse grid (typically on the order of $8 \times 8 \times 8$) of electron and phonon momenta.

The development of the method for interpolation of electron-phonon coupling constants obtained on a coarse grid to a dense grid [6] was a crucial step toward enabling calculations of phonon-limited mobility. The method is based on the transformation between the reciprocal space representation and the local representation. While the relevant quantities in the reciprocal space representation are the coupling parameters between the Bloch electronic states with quasimomentum $\mathbf{k}$ and phonon modes with quasimomentum $\mathbf{q}$, in the local representation one uses the coupling parameters between localized electronic orbitals (where typically Wannier functions are used as localized orbitals) due to displacements of individual atoms. The electron-phonon coupling constants on a coarse grid in reciprocal space representation are therefore first transformed to a local representation. Using these parameters in the local representation one can then calculate the electron-phonon coupling constants in the reciprocal space representation for arbitrary wave vectors of electrons $\mathbf{K}$ and phonons $\mathbf{Q}$, not only those from the original coarse grid. First studies of carrier mobility in semiconductors using this approach [7–9] or somewhat different approach [10] were focused on silicon, the most well-known semiconducting material.

The method in this form, however, implicitly contains the assumption that the electron-lattice coupling parameters in the local representation are short ranged, i.e., that the potential change caused by the displacement of an atom in a

*nenad.vukmirovic@ipb.ac.rs

certain direction is short ranged. This is not the case in polar semiconductors where each atom carries an effective charge (so-called Born effective charge), which creates a long-ranged potential when the atom is displaced from its equilibrium position. This issue was overcome using the approach developed in Refs. [11] and [12]. The main idea of the approach is to remove the long-ranged part of electron-lattice coupling parameters caused by the potential of Born effective charges, perform the interpolation starting from short-ranged parameters, and return the long-ranged part at the end. This approach was used in the calculations of mobility for the most representative polar semiconductor GaAs [8,13,14]. Other materials that have been studied afterwards include GaN [15,16], diamond [17], halide perovskites [18], SnSe [19], SiC [20] (for a review of these works see Ref. [21]). There have been also other works where *ab initio* calculations were used to some extent to study the mobility in semiconductors [22–26].

Studies of mobilities in other semiconducting materials are necessary to further verify or improve the whole approach. In this work, we focus on II-VI semiconductors with the formula AB, where A is Zn or Cd, while B is Se or Te. These are well-established semiconductor materials with a wide range of applications including solar cells, x-ray, and γ-ray detectors, infrared optical materials, etc. [27]. We perform calculations of temperature dependence of the mobility of electrons in these materials. We include in the procedure the corrections to known shortcomings of local approximations to density functional theory, such as inaccurate band dispersion and overscreening. It turns out that these corrections are necessary to obtain the mobilities that are in good agreement with experimental results from the literature. Finally, we analyze different contributions to the mobility and identify simpler models that can be used to obtain reasonably accurate values of the mobility at a smaller computational cost.

The paper is organized as follows. In Sec. II we give an overview of the methodology that we used to calculate the electron mobility in the material. The results of our calculations are given in Sec. III with electronic structure presented in Sec. III A and the results for phonons, electron-phonon coupling constants, Born-effective charges, and dielectric constants given in Sec. III B. The comparison of calculated mobilities with experimental results from the literature is performed in Sec. III C and the results for mobility using different models are given in Sec. III D. Final remarks are presented in Sec. IV.

II. METHODOLOGY

The methodology that we used to obtained the electron mobility in the material consists of the calculation of electronic structure and construction of Wannier functions, interpolation of electron-lattice coupling constants from a course to a dense momentum grid, calculation of phonons and finally the calculation of electron mobility.

Density functional theory is used to obtain the wave functions of electronic states and corresponding energies. The wave functions obtained are then used to construct the localized Wannier functions [28], i.e., the unitary matrices that describe the transformation from the delocalized Bloch wave functions to localized Wannier functions. With these matrices at hand one obtains the single-particle Hamiltonian in the Wannier basis, which can then be diagonalized to obtain the wave functions and energies at arbitrary point in the Brillouin zone, not only the ones from the original grid of electronic wave vectors. The steps just described constitute the procedure for Wannier interpolation of electronic band structure. Mathematical details of this procedure are given in Sec. I A of the Supplemental Material [29].

Fourier-Wannier interpolation procedure [6] is used next to perform the interpolation of electron-lattice coupling constants. These constants are obtained first from a density functional perturbation theory calculation on a coarse grid in reciprocal space. The long-ranged part of these constants is then removed following the ideas of Refs. [11] and [12]. In these works, the most important dipole contribution is considered and we note in passing that most recent studies [30,31] have addressed the possibility of including additional quadrupole terms. The transformation of electron-lattice coupling constants to localized Wannier representation is performed next using the same unitary matrices obtained during Wannier interpolation of electronic band structure. In the following step, these constants are transformed back to reciprocal space representation, where these can be obtained now for arbitrary wave vectors, not only for those from original coarse grid. In the final step, long-ranged part of electron-lattice coupling constants is put back. In this step, we allow also for the possibility to correct the long-ranged part of these constants by using the corrected values of high-frequency dielectric constants or Born effective charges. Mathematical details of this procedure that include also comments on some differences of our implementation in comparison to previous works are given in Sec. I B of Supplemental Material [29].

The dynamical matrices, the phonon energies and the displacements of phonon modes on the coarse phonon wave vector grid are obtained from density functional perturbation theory. Interpolation of dynamical matrices to arbitrary phonon wave vectors is performed in a standard manner (see, for example, Refs. [4,5]) by (i) removing the long-ranged part of dynamical matrices; (ii) transforming short-ranged part of dynamical matrices to force constant representation; (iii) evaluating the short-ranged part of dynamical matrices on the dense grid; (iv) putting back the long-ranged part of dynamical matrices; (v) obtaining the phonon energies and displacements from the eigenvalue problem of dynamical matrices. As in the case of electron-phonon coupling constants, we allow here for the possibility to introduce the corrected dielectric constants and Born effective charges in step (iv) of the procedure.

In this work we consider the electrons in the conduction band and assume that the concentration of electrons is relatively low. The mobility obtained this way can be considered as representative mobility of electrons in the conduction band of the material. Within the momentum relaxation time approximation, the components of the charge carrier mobility tensor are given by the expression [32]

$$\mu_{ij} = -e_0 \frac{\sum_{\mathbf{K}} v_{\mathbf{K}}^{(i)} v_{\mathbf{K}}^{(j)} \tau_{\mathbf{K}} \frac{\partial f_{\mathbf{K}}}{\partial \varepsilon_{\mathbf{K}}}}{\sum_{\mathbf{K}} f_{\mathbf{K}}}. \quad (1)$$

In this equation $f_{\mathbf{K}}$ is the population of the state at wave vector $\mathbf{K}$ given by the Maxwell-Boltzmann distribution $f_{\mathbf{K}} \propto e^{-\frac{1}{k_B T}\tilde{\varepsilon}_{\mathbf{K}}}$, $\tilde{\varepsilon}_{\mathbf{K}}$ is its energy, $v_{\mathbf{k}}^{(i)}$ are the components of group velocity $v_{\mathbf{K}}^{i} = \frac{1}{\hbar}\frac{\partial \tilde{\varepsilon}_{\mathbf{K}}}{\partial K_i}$, e_0 is the elementary charge, T is the temperature, while $\tau_{\mathbf{K}}$ is the momentum relaxation time. In the limit of low carrier concentration considered here, this time is given as

$$\frac{1}{\tau_{\mathbf{K}}} = \frac{2\pi}{\hbar N_{\mathbf{Q}}} \sum_{\mathbf{Q}} \sum_{\lambda,\pm} |\gamma^{\lambda}(\mathbf{K},\mathbf{Q})|^2 \left(n_{\lambda\mathbf{Q}} + \frac{1}{2} \mp \frac{1}{2} \right) \times \delta(\tilde{\varepsilon}_{\mathbf{K}} \pm \hbar\omega_{\lambda\mathbf{Q}} - \tilde{\varepsilon}_{\mathbf{K}\pm\mathbf{Q}})(1 - \cos\theta_{\mathbf{K},\mathbf{K}\pm\mathbf{Q}}). \quad (2)$$

In the previous equation $\gamma^{\lambda}(\mathbf{K},\mathbf{Q})$ is the electron-phonon coupling element for scattering of an electron in state $\mathbf{K}$ to the state $\mathbf{K} \pm \mathbf{Q}$ due to interaction with phonon in mode λ with wave vector $\mathbf{Q}$, $\hbar\omega_{\lambda\mathbf{Q}}$ is the energy of that phonon, $n_{\lambda\mathbf{Q}}$ is the occupation of that phonon state given by the Bose-Einstein distribution, while $N_{\mathbf{Q}}$ is the number of points on the dense reciprocal space grid. The term $\cos\theta_{\mathbf{K},\mathbf{K}\pm\mathbf{Q}}$ is given as

$$\cos\theta_{\mathbf{K},\mathbf{K}\pm\mathbf{Q}} = \frac{\mathbf{v}_{\mathbf{K}} \cdot \mathbf{v}_{\mathbf{K}\pm\mathbf{Q}}}{|\mathbf{v}_{\mathbf{K}}| \cdot |\mathbf{v}_{\mathbf{K}\pm\mathbf{Q}}|}. \quad (3)$$

Band indices were omitted in previous equation because only the states at the bottom of the conduction band are relevant in this work.

III. RESULTS

A. Electronic structure

Density functional theory calculations of the electronic structure were performed either by approximating the exchange-correlation functional using the Perdew-Burke-Ernzerhof (PBE) generalized gradient approximation (GGA) [33] or by using the hybrid Heyd-Scuseria-Ernzerhof (HSE06) functional [34,35]. The effect of spin-orbit interaction was not included since we focus on the electronic states in the conduction band that mainly originate from s atomic orbitals. Calculations were performed using the ABINIT code [36,37]. The effect of core electrons was modeled using optimized norm-conserving scalar relativistic Vanderbilt pseudopotentials [38,39]. Kinetic energy cutoff for plane-wave representation of the wave functions was 35 Ha for ZnSe and ZnTe, and 40 Ha for CdSe and CdTe, while the $8 \times 8 \times 8$ Monkhorst-Pack grid of points in reciprocal space was used. Experimental lattice constants at room temperature taken from Ref. [40] were used in all calculations. Their values are summarized in Table I.

Wannier functions were constructed from 18 Bloch bands. The top eight valence bands and the lowest ten conduction bands were used to construct ten localized Wannier functions. We have used the procedure for construction of localized Wannier functions for entangled energy bands [41] whereas the Bloch states that lie within the energy window containing the top three valence bands and the bottom conduction band were left unchanged in the band disentanglement procedure (this energy window is called the frozen energy window in terminology of Ref. [42]). Calculations of the unitary matrices that connect the Bloch functions and the Wannier functions (Eq. (2) in Supplemental Material [29]) were performed using the WANNIER 90 code [42]. In Sec. II of Supplemental Material [29] we compare the band structure obtained using direct DFT calculation with the band structure obtained by Wannier interpolation. The results suggest that the dispersion of the first conduction band, which is the relevant band in this study is excellently reproduced by Wannier interpolation.

TABLE I. Lattice constants used in the calculation and effective masses and band gaps obtained from electronic structure calculations. a_0 (expt) denotes the experimental value of the lattice constant taken from Ref. [40]. m_{eff} (m_0) denotes the conduction band effective mass in units of free electron mass m_0, while E_g denotes the band gap. The label (expt) denotes experimental values of effective masses and gaps taken from the compilation in Ref. [27], while the labels (PBE) and (HSE06) denote our calculations using the PBE and HSE06 functional.

	ZnSe	ZnTe	CdSe	CdTe
a_0 (Å) (expt)	5.667	6.0882	6.078	6.482
m_{eff} (m_0) (expt)	0.137	0.117	0.119	0.090
m_{eff} (m_0) (PBE)	0.096	0.087	0.061	0.064
m_{eff} (m_0) (HSE06)	0.14	0.13	0.13	0.13
E_g (eV) (expt)	2.72	2.27	1.68	1.51
E_g (eV) (PBE)	1.29	1.28	0.61	0.77
E_g (eV) (HSE06)	2.32	2.19	1.53	1.61

Calculated band structure of ZnSe along several high-symmetry directions is presented in Fig. 1, while the plot for three other materials that we considered is given in Supplemental material [29] (Sec. III therein). Since we focus on electronic transport in the conduction band, which is strongly influenced by the conduction band effective mass, it is instructive to assess the accuracy of effective masses obtained. For this reason, we compare in Table I the conduction band effective mass obtained from our calculations to the experimental effective mass. The results indicate that the PBE functional significantly underestimates the effective masses. On the other hand, the HSE06 functional gives rather accurate effective masses for ZnSe, ZnTe, and CdSe (interestingly the effective

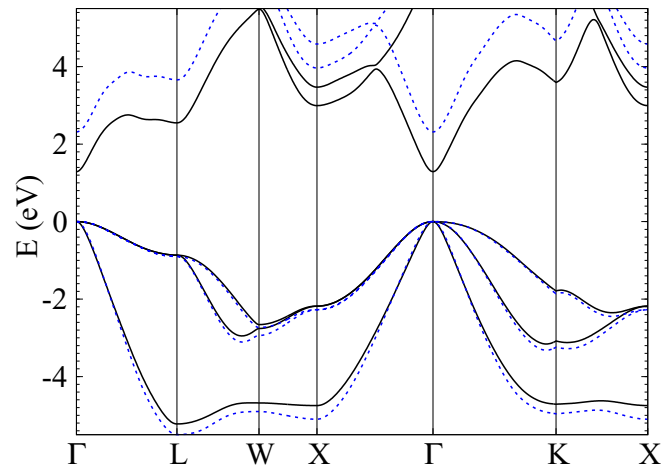

FIG. 1. Electronic band structure of ZnSe calculated using the PBE functional (full line) and the hybrid HSE06 functional (dashed line).

masses of the three materials are rather similar; experimental ones differ by no more than 0.02 m_0, while the HSE06 values differ by no more than 0.01 m_0), while it overestimates the effective mass of CdTe. These facts should be born in mind in the analysis of electron mobility results, which is the main focus of this work.

Next, we discuss the need to use the density functional, which yields reasonably accurate values of the band gap. At first thought, this does not seem to be important because the relevant states for electron mobility are the states at the bottom of the conduction band and the value of the material band gap is not relevant for transport properties in the conduction band. The calculated values of the band gap are nevertheless presented in Table I. We see that the HSE06 gaps agree much better with experiment than the PBE gaps, which are too small due to the well-known band gap problem [43] of local and semilocal approximations for exchange-correlation functional in DFT. On the other hand, it has been previously established that HSE06 functional yields quite accurate values of the band gap [44]. We therefore see that both effective masses and band gaps are underestimated in PBE calculations. Such a result could have been expected based on an approximate perturbative formula that connects the conduction band effective masses and the band gap as (see, for example, Ref. [45], p. 12)

$$\frac{1}{m_{\text{eff}}} = \frac{1}{m_0} + \frac{2P^2}{\hbar^2 E_g}, \tag{4}$$

with the matrix element P given as $P = \frac{\hbar}{m_0}\langle S|p_x|X_v\rangle$, where $|S\rangle$ is the conduction band Bloch state at Γ, p_x is the operator of the x component of the momentum, while $|X_v\rangle$ is the top valence band state at Γ that transforms as x under the operation of the symmetry group of the crystal. We see from Eq. (4) that the underestimation of the gap is likely to lead to the underestimation of the conduction band effective mass. As a consequence, to obtain reasonably good conduction band effective masses, one needs to obtain reasonably good band gaps as well.

B. Phonons, electron-phonon coupling constants, Born effective charges, and high-frequency dielectric constants

The calculation of phonons and electron-lattice coupling constants on the coarse $8 \times 8 \times 8$ Monkhorst-Pack grid was also performed using the ABINIT code [36,37]. The PBE exchange-correlation functional was used in the calculation. The phonon band structure of ZnSe obtained from the calculation and subsequent interpolation is presented in Fig. 2, while the phonon band structure of the other materials considered is given in Supplemental Material [29] (Sec. IV therein). We note that HSE06 dielectric constants were used to correct the long-ranged part of the dynamical matrix, as mentioned in Sec. II. The comparison of phonon energies at characteristic points in the Brillouin zone in the cases when this correction was included and excluded with experimental results is given in Tables I–IV in Sec. IV of Supplemental Material [29]. These results suggest that differences between the results obtained in the two cases are rather small and that the results of the calculation agree well with experiment. Namely, the largest difference between the calculation with correction and

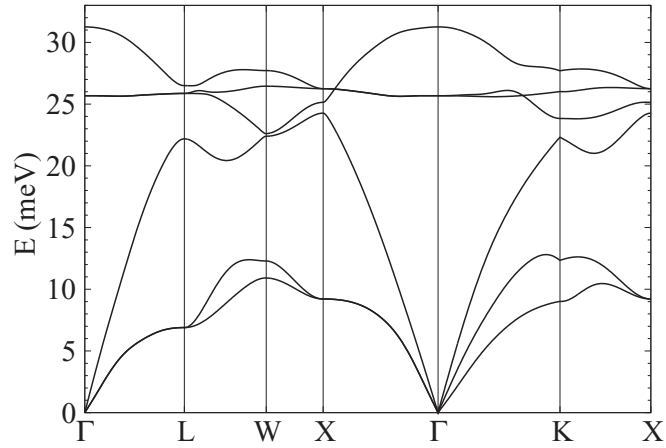

FIG. 2. Phonon band structure of ZnSe.

experiment is 1.3 meV, the largest difference between the calculation without correction and experiment is 1.7 meV, while the largest difference between calculations with and without correction is also 1.3 meV.

The electron-phonon coupling constants [defined after Eq. (2)] obtained from the interpolation procedure are presented in Fig. 3 in the case of ZnSe, and in Supplemental Material [29] (Sec. V therein) for other materials. The interpolation procedure was performed using our in-house code that uses as input the output of DFT and DFPT calculations performed using ABINIT. As a check of accuracy of our implementation of interpolation procedure, we show in Sec. VI of Supplemental Material [29] the comparison of electron-lattice coupling elements obtained directly from DFPT (circles in these figures) and those obtained after interpolation (full line in these figures).

The most relevant electronic states for electronic transport are those in the vicinity of the Γ point. For this reason we present the electron-phonon coupling constants for scattering

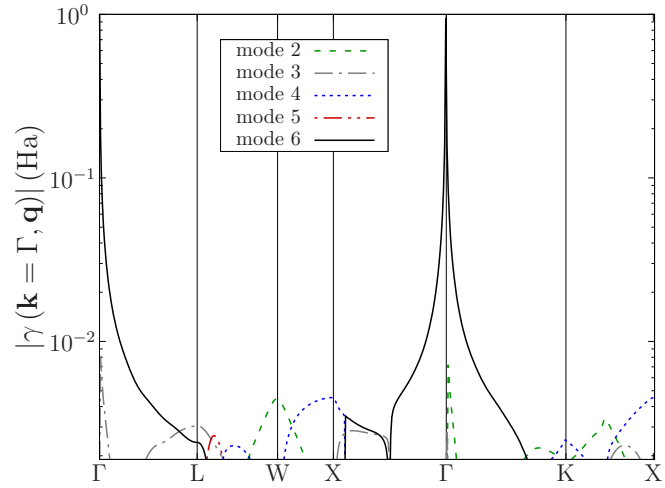

FIG. 3. Electron-phonon coupling constants (obtained from the interpolation procedure) for scattering of an electron at wave vector $\mathbf{k} = \Gamma$ with a phonon of a given mode at wave vector $\mathbf{q}$ in ZnSe. The modes are labeled in ascending order of their energies at $\mathbf{q}$.

TABLE II. High-frequency dielectric constants and Born effective charges obtained from the calculations using the PBE and HSE06 functional and experimental data for dielectric constants. Experimental data were taken from Ref. [27] where an average is taken from the values obtain from different sources.

	ZnSe	ZnTe	CdSe	CdTe
ε_r^∞ (expt)	5.9	6.9	6.2	7.1
ε_r^∞ (PBE)	7.26	8.86	7.72	8.62
ε_r^∞ (HSE06)	6.15	7.45	6.13	7.01
Z (PBE)	2.05	2.00	2.23	2.18
Z (HSE06)	2.09	2.05	2.24	2.18

of an electron at Γ with phonon of different wave vectors **q**. The most relevant among these are the coupling constants at low $|\mathbf{q}|$ because only these phonons can satisfy the energy conservation law for scattering between two electronic states in the vicinity of Γ. As can be seen from Fig. 3, in this region of electron and phonon wave vectors, by far the largest electron-phonon coupling constants, are those with highest energy phonon mode, which is the longitudinal optical (LO) phonon mode. One might even be tempted to conclude from Fig. 3 that the interaction of an electron with phonons in other modes could be completely neglected. However, one should bear in mind that at low temperatures, the number of phonons in high-energy modes decreases exponentially, which leads to a strong reduction of electron-phonon scattering rate. We note that our work does not consider the effect of screening of electron-phonon interaction that becomes important for higher concentration of carriers [46,47].

We next discuss the values of Born effective charges and high-frequency dielectric constants. Since these appear directly in the expression for long-ranged part of the electron-phonon interaction, one should pay particular attention to accuracy of their values. Within PBE approximation to DFT we have calculated the Born effective charges and high-frequency dielectric constants using two different methods: (i) using density functional perturbation theory [5]; (ii) by performing the calculation of polarization and atomic forces in finite electric field [48,49] and extracting the slope of the dependence of these quantities on field at low fields. In calculations that used the HSE06 functional, we have performed only the calculation using the method (ii) due to higher computational cost of hybrid functional calculations and a lack of code that implements DFPT calculation with hybrid functionals. All calculations were performed using the ABINIT code, while additional technical details of the calculations are given in Supplemental Material [29] (Sec. VII therein). We emphasize that larger grids in reciprocal space than those used to obtain the band structure are needed to obtain converged values of dielectric constants. The results of the calculations are summarized in Table II. The results indicate significant differences between dielectric constants obtained using PBE and HSE06 and show that HSE06 results are in much closer agreement with experiment. On the other hand, Born effective charges calculated using the two functionals are very similar. Consequently, we set ε_{r1}^∞ in Eq. (9) in Supplemental Material [29] to the value obtained using PBE and we set ε_{r2}^∞ in Eq. (17) in Supplemental Material [29] to the value obtained using HSE06, while we set both Z_1 and Z_2 in these equations to the value obtained using PBE. The difference between dielectric constants obtained using the two functionals originates from the fact that dielectric constants describe the screening of the electric field, which is sensitive to the functional used. On the other hand, the Born effective charges defined as the restoring force on an atom in a unit electric field are largely a local property and appear to be rather insensitive to the functional used.

C. Mobility: Comparison with experiment

Next, we present the calculated temperature dependence of the mobility for the materials under consideration. The mobility was calculated using Eq. (1). The summation was performed over **K** points from a 120 × 120 × 120 Monkhorst-Pack grid, where only the points that satisfy the condition $\tilde{\varepsilon}_{\mathbf{K}} - \varepsilon_{\min} < \varepsilon_c$ were taken, where $\varepsilon_{\min}$ denotes the energy of the conduction band minimum. The value of $\varepsilon_c = 250$ meV is sufficient to get converged results at all temperatures considered. Detailed convergence checks with respect to the size of the **K** points grid and with respect to the value of ε_c are presented in Supplemental Material [29] (Secs. VIII and IX therein). The sums in Eq. (2) containing the δ function were transformed to integrals that were calculated using the tetrahedron method [50,51]. All calculations were performed using our in-house code. Our calculations are based on the momentum relaxation time approximation [Eqs. (2) and (1)]. For this reason, we have estimated the accuracy of this approximation by comparing the results with the full solution of Boltzmann equations in the case of the model with parabolic bands and Fröhlich electron-phonon coupling with a single dispersionless phonon mode. The results of the comparison are presented in Sec. X in Supplemental Material [29]. The results suggest that the error introduced due to momentum relaxation time approximation is smaller than 5% at room temperature and smaller than 30% at lowest temperatures considered. The conclusion in this regard is similar as the conclusion for GaAs in Ref. [8] where the error of momentum relaxation time approximation was also small at higher temperatures and increased as the temperature decreased.

Calculated temperature dependence of the mobility in ZnSe is presented in Fig. 4 along with experimental data from Refs. [52–58]. It can be seen from Fig. 4 that the results obtained when PBE functional is used throughout the calculation significantly overestimate the experimental results. Two main reasons of this overestimation can be identified. We have shown in Sec. III A that the PBE functional calculations underestimate the effective masses. This leads to overestimate of the mobility since lower effective masses are beneficial for efficient charge transport and therefore lead to higher mobilities. In Sec. III B, we have demonstrated that ε_r^∞ obtained from PBE is larger than the experimental one. Since the long-ranged part of electron-phonon interaction is inversely proportional (see Eq. (17) in Supplemental Material [29]) to ε_r^∞, it follows that overestimate of ε_r^∞ leads to underestimate of electron-phonon scattering matrix elements. Smaller scattering is also beneficial for charge transport and therefore larger mobility is obtained in the calculation.

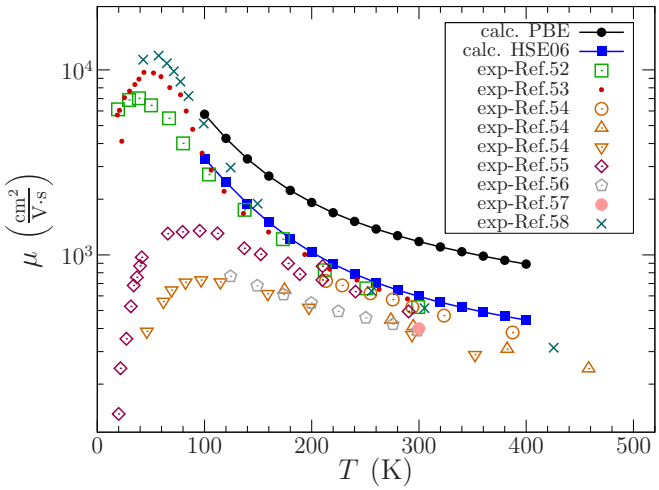

FIG. 4. Temperature dependence of electron mobility in ZnSe. The label "calc. PBE" denotes the calculation where PBE exchange correlation functional is used throughout the calculation, while "calc. HSE06" denotes the calculation where energies and dielectric constants obtained using PBE are replaced with those obtained using HSE06. Experimental data from Refs. [52–58] are given for comparison.

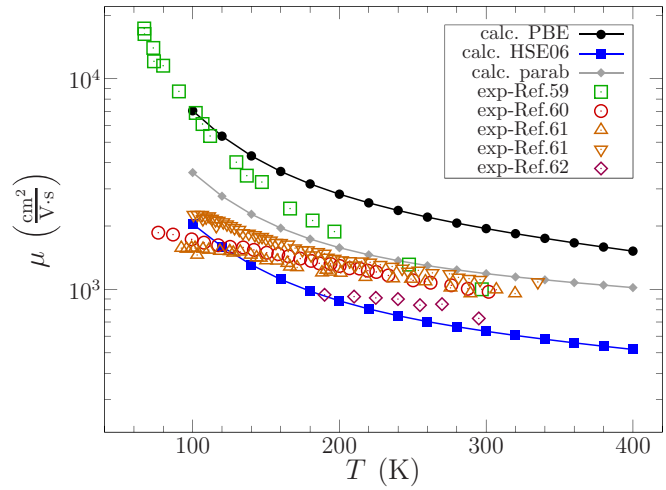

FIG. 5. Temperature dependence of electron mobility in CdTe. The label "calc. PBE" denotes the calculation where PBE exchange correlation functional is used throughout the calculation, "calc. HSE06" denotes the calculation where energies and dielectric constants obtained using PBE are replaced with those obtained using HSE06, while "calc. parab." denotes the calculation where parabolic band structure with experimental effective mass is used along the HSE06 dielectric constants. Experimental data from Refs. [59–62] are given for comparison.

To overcome the limitations of the PBE functional, we performed the calculations where more accurate conduction band structure and ε_r^∞ are used in the calculation. More precisely, to improve the conduction band structure, we change in the diagonal matrix $h_d(\mathbf{k})$ in Eq. (3) in Supplemental Material [29] the eigenenergies obtained by PBE with those obtained in HSE06 calculation. To obtain a better description of the screening of the long-ranged part of the electron-phonon interaction, we set ε_{r2}^∞ in Eq. (17) in Supplemental Material [29] to the value obtained using HSE06 instead of the value ε_{r1}^∞ obtained using PBE that is used in Eq. (9) in Supplemental Material [29]. For brevity, we refer to these calculations as HSE06 calculations, although we note that this does not mean that full DFPT calculation with HSE06 functional was performed. The results obtained in such a calculation are also shown in Fig. 4. It can be seen from the figure that the level of agreement of these results with experimental data from the literature becomes much better, as will be discussed in what follows.

The agreement between HSE06 calculation and experiment is rather good for experimental results presented in Ref. [52] (the high mobility sample in Fig. 4 therein) that concern high-quality samples of ZnSe grown by molecular beam epitaxy. The same is the case regarding the results of Ref. [53] (Fig. 3 therein). The calculation results are also only slightly larger than the measurement results on the highest mobility sample in Ref. [54] (Fig. 5 therein), while two other samples in Ref. [54] have lower mobilities (these are also presented in our Fig. 4) suggesting that nonintrinsic scattering mechanisms could be present. Our calculation results are somewhat larger than the experimental data in Ref. [55] [Fig. 2(b) therein] in the temperature range between 200 K and 300 K. At lower temperatures experimental data of Ref. [55] show a decrease of mobility with decreasing temperature, which is a signature of the effects of impurity scattering and for this reason comparison of our calculation with experiment would not be meaningful in this temperature range. The experimental results of Refs. [56] (Fig. 1 therein) and [57] (Table I therein) are noticeably smaller than the results of our calculation, even around room temperature, suggesting that these samples could be of somewhat lower quality than the samples previously considered. Our calculation results are also in reasonably good agreement with the results of Ref. [58] except at the lowest temperatures (around 100 K) where, surprisingly, larger values of mobility are obtained in experiment. We note that this is the region where the concentration of carriers (and therefore the current in the experiment) is rather small and that the origin of the difference could potentially be the issues with accurate measurements of small currents. Overall, Fig. 4 suggests that HSE06 calculation results are at the upper limit of the results obtained in experiments and are in agreement with the experimental results obtained on highest purity and highest mobility samples.

Next, we turn our attention to the CdTe material and compare in Fig. 5 the results of our calculations with experimental data from Refs. [59] (highest mobility sample in Fig. 1 therein), [60] (highest mobility sample in Fig. 3 therein), [61] (Figs. 2 and 6), [62] (Fig. 3). As in the case of ZnSe, PBE calculation gives higher mobility than the HSE06 calculation due to differences in effective masses and dielectric constants predicted by two different functionals. The HSE06 results in the region of temperatures near 300 K are lower than experimental results. To understand why this is the case, we recall from Table I that HSE06 effective mass of CdTe is larger than experimental effective mass. For this reason, the calculation that uses the HSE06 band structure underestimates the material mobility. On the other hand, the PBE calculation where effective mass is underestimated overestimates the mobility. Such results point to the necessity of accurately describing

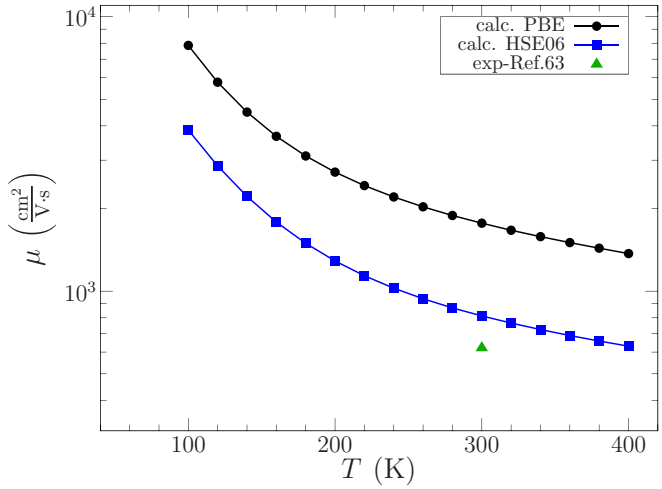

FIG. 6. Temperature dependence of electron mobility in ZnTe. The label "calc. PBE" denotes the calculation where PBE exchange correlation functional is used throughout the calculation, while "calc. HSE06" denotes the calculation where energies and dielectric constants obtained using PBE are replaced with those obtained using HSE06. Experimental data from Ref. [63] are given for comparison.

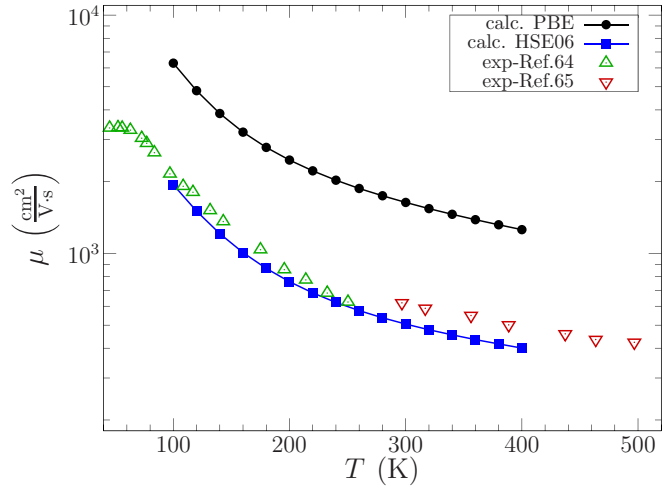

FIG. 7. Temperature dependence of electron mobility in CdSe. The label "calc. PBE" denotes the calculation where PBE exchange correlation functional is used throughout the calculation, while "calc. HSE06" denotes the calculation where energies and dielectric constants obtained using PBE are replaced with those obtained using HSE06. Experimental data from Refs. [64,65] are given for comparison.

the band curvature near the bottom of conduction band (i.e., the conduction band effective mass) for accurate prediction of electron mobility. To confirm that this is the case, we performed an additional calculation where a parabolic band structure with experimental effective mass was assumed. As expected, this calculation gives a rather good agreement with experiment at temperatures around the room temperature, see Fig. 5. Nevertheless, one should note that the calculation can no longer be considered as an *ab initio* calculation if the band structure obtained from experimental effective mass is used in the calculation.

We consider next the ZnTe material. Experimental data for mobility in n-type ZnTe are rather scarce probably because n-type doping of ZnTe is rather difficult [40]. We compare in Fig. 6 our HSE06 result with the results of Ref. [63] (the point at lowest concentration in Fig. 2 therein) and obtain reasonably good agreement. As in the case of other materials, our PBE results are significantly larger than HSE06 results.

Finally, we discuss the results obtained for CdSe. The comparison of our calculation results with experimental data from Refs. [64] (Fig. 3) and [65] (Fig. 2) is presented in Fig. 7. Our HSE06 calculation results closely follow the results of Ref. [64] and are somewhat smaller than the results of Ref. [65]. It should be noted that our calculations concern the zincblende form of CdSe, while it has been reported that experimental data correspond to wurtzite form of CdSe. However, the arrangement of atoms and the distances between them in two forms of CdSe are rather similar and the values of most relevant material parameters (such as the conduction band effective mass, the high-frequency dielectric constant, the band gap, the optical phonon energies, and the material density) are also rather similar (see, for example, Ref. [27] for the values of these parameters in wurtzite and zincblende CdSe). For this reason, the comparison of our results with experimental data could be meaningful.

It is evident from previous results that better results for mobility were obtained by introducing two corrections: the correction to the dielectric constant and the correction to the band structure. It is instructive to assess the importance of each of the two corrections. For this reason, we have also performed the calculations where only one of these corrections was included. The results presented in Sec. XI of Supplemental Material [29] indicate that correction to the band structure is larger and that both contributions are significant. For example, in the case of ZnSe, the correction to the dielectric constant reduces the room-temperature mobility by a factor of approximately 1.25, while the correction to the band structure reduces it by a factor of 1.6, yielding a total reduction by approximately a factor of 2.

We note that all our calculations concern the drift mobility μ_d of electrons in the material, while most of the experiments report the Hall mobility μ_H. The two are related as $\mu_H = r_H \mu_d$, where r_H is the so-called Hall factor. A good estimate of the Hall factor can be obtained from a result derived for a parabolic band that reads (see, for example, Ref. [32], p. 196)

$$r_H = \frac{\langle \varepsilon \rangle \cdot \langle \varepsilon \cdot \tau^2 \rangle}{\langle \varepsilon \cdot \tau \rangle^2}, \tag{5}$$

where ε is the energy of the carrier with respect to the bottom of the conduction band, τ is the momentum relaxation time, and the averages are defined as $\langle x \rangle \equiv \frac{\sum_{\mathbf{k}} f_{\mathbf{k}} x}{\sum_{\mathbf{k}} f_{\mathbf{k}}}$. We expect that this is a good estimate for the materials at hand because the bottom of the conduction band can be well approximated to be parabolic. We have calculated r_H using Eq. (5) for all materials that we considered throughout the whole range of temperatures and we have found that r_H is within the range (1.03,1.17), while corresponding values at four different temperatures for all material considered are given in Sec. XII of Supplemental Material [29]. Since it only slightly deviates

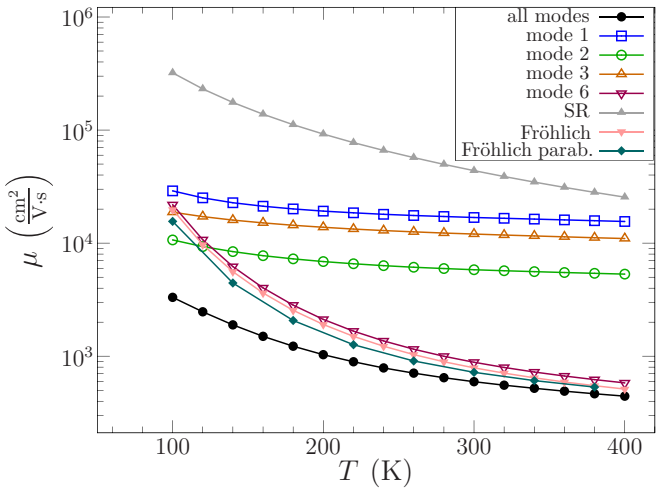

FIG. 8. Temperature dependence of mobility in ZnSe: different contributions and the results from different models. The label "all modes" denotes the results when all phonon modes are included, while the labels "modes 1–6" denote the results when only a particular phonon mode is included. The phonon modes are numbered in ascending order of their energies. The label "SR" concerns the results where only short-ranged part of electron-phonon coupling is included. The label "Fröhlich" denotes the results where only mode 6 is included and where Fröhlich model for electron-phonon coupling is used. The label "Fröhlich parab." refers to the previous case where the band energies are replaced with those obtained from a parabolic band dispersion model.

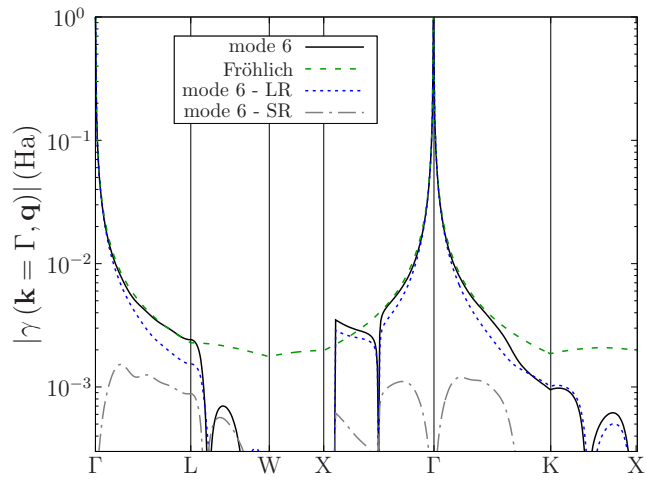

FIG. 9. Electron-phonon coupling constants for scattering of an electron at wave vector $\mathbf{k} = \Gamma$ with a mode 6 phonon at wave vector $\mathbf{q}$ in ZnSe. The label "mode 6" denotes the results of the full calculation, "mode 6 - LR" and "mode 6 - SR" denote its long-ranged and short-ranged part, while the label "Fröhlich" denotes the result for the Fröhlich model.

from the value of 1 the comparison of calculated drift mobilities with experimental Hall mobilities is fully appropriate.

D. Mobility: Results of different models

Next, we analyze different contributions to the total mobility of the material and use the results obtained to consider the possibility to obtain accurate mobility results without performing the whole procedure of evaluating electron-phonon coupling constants on a dense reciprocal space grid.

In Fig. 8 we plot the results that are obtained when only one phonon mode is included in the calculation. The results indicate that mobility in the presence of scattering at longitudinal optical phonons (mode 6) is very similar to the total mobility at temperatures around the room temperature. This implies that LO-phonon scattering is the dominant scattering mechanism at these temperatures. At low temperatures, the mobility in the presence of scattering at acoustic phonons (modes 1–3) becomes comparable or even smaller than the mobility in the presence of LO-phonon scattering. These modes then provide the dominant scattering mechanism (We note that in realistic samples at low temperatures or at high impurity concentration one should as well consider impurity scattering as an important scattering mechanism). Such a behavior is fully expected and has been identified starting from the early studies [66] of transport in these materials. The origin of such a behavior comes from the fact that at low temperatures there are very few LO phonons and very few electrons at the states from which LO phonon emission could be possible.

Given the fact that mobility is mostly determined by LO phonon scattering at higher temperatures, it is interesting to consider if the same results could be obtained using some relevant model for electron-phonon interaction without performing the evaluation of electron-phonon coupling constants on the dense grid. The model that is expected to provide a reasonably good description of the interaction between electrons and LO phonons is the Fröhlich model since we consider direct band gap materials where all relevant electronic states are at the vicinity of the Γ point and no intervalley scattering effects are relevant. Within the Fröhlich model, the electron-phonon coupling constant is given as

$$|\gamma(\mathbf{k},\mathbf{q})|^2 = \frac{\hbar e_0^2 \omega_{\text{LO}}}{2V\varepsilon_0}\left(\frac{1}{\varepsilon_r^{\infty}} - \frac{1}{\varepsilon_r^{\text{st}}}\right)\frac{1}{q^2}, \tag{6}$$

where $\hbar\omega_{\text{LO}}$ is the LO phonon energy, V is the volume of the primitive cell of the crystal and $\varepsilon_r^{\text{st}}$ is the static relative dielectric constant. The values of the parameters used in the Fröhlich model are summarized in Supplemental Material [29] (Sec. XIII). The results obtained with electron-phonon coupling from Eq. (6) and by taking into account only the LO phonon mode are also shown in Fig. 8 (labeled as "Fröhlich"). These results are very similar to the results obtained when only mode 6 is considered and consequently they are close to the full mobility results at higher temperature when mode 6 provides the dominant scattering mechanism. To better understand the origin of such a good agreement we compare in Fig. 9 the electron-phonon coupling constants for mode 6 in the full calculation and within the Fröhlich model. The figure shows that the long-ranged part of electron-phonon interaction dominates over the short-ranged part and that it nicely matches the Fröhlich model in the relevant range of $\mathbf{q}$ vectors around the Γ point.

The agreement between electron-phonon coupling constants further leads to the agreement in scattering times. In Fig. 10 we present the dependence of scattering time on carrier

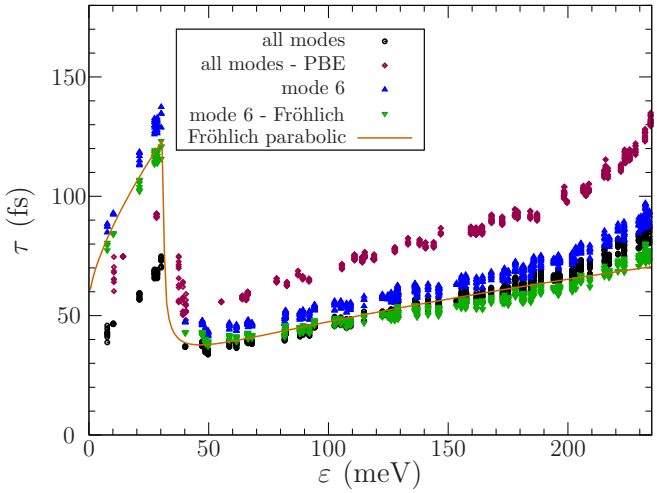

FIG. 10. Dependence of momentum relaxation time on electron energy at a temperature of $T = 300$ K in ZnSe. The label "all modes" denotes the results of the full calculation, the label "all modes - PBE" refers to the results of the full calculation when PBE functional is used, the label "mode 6" denotes the results when only phonon mode 6 is included, the label "mode 6 - Fröhlich" denotes the results for the Fröhlich model for mode 6, while the label "Fröhlich parabolic" denotes the results for the Fröhlich model with parabolic band structure.

energy with respect to the bottom of the conduction band. There is an overall good agreement between the scattering time due to mode 6 and the scattering times in the Fröhlich model. The scattering times caused by all phonon modes differ from these at low energies where LO phonon emission is not possible and where main contribution therefore comes from acoustic phonons. Due to this difference, it is not possible to accurately predict mobility at lower temperatures using a model that includes LO phonons only. All conclusions stemming from Figs. 8, 9, and 10 carry over to other materials, while analogous figures are given in Supplemental Material [29] (Secs. XIV, XV, and XVI therein).

We also note that the results indicate that the momentum relaxation times increase when electron energy increases except in the region around LO phonon energy when phonon emission events become energetically allowed. There are two opposing factors that determine the dependence of momentum relaxation time on electronic energy. On the one hand, for larger energy, the phase space for scattering increases and for this reason one would expect the momentum relaxation time to decrease. On the other hand, for larger energy, the phonon momenta involved in a scattering event become larger on average (when electron energy is sufficiently large that LO phonon emission is possible) and hence the scattering matrix element becomes smaller, an effect that would lead to an increase of momentum relaxation time. Which of these two opposing effects will prevail can be concluded with certainty only from a full calculation. In Sec. XVII of the Supplemental Material [29] we show an analytic expression in the case of the Fröhlich model with parabolic band structure. The results of this model (shown in Fig. 10 and in Figs. 42–44 in Supplemental Material [29]) exhibit essentially the same behavior as the results of the full calculation. Such an agreement is certainly not expected to extend to large energies above the bottom of the conduction band. For example, it was shown in Ref. [67] that in GaN the scattering rates from the Fröhlich model agree with full calculation up to energies of ∼150 meV above the bottom of the conduction band, while in the case of GaAs this agreement cannot extend up to more than ∼250 meV when L valley states start to play a role [13]. We find that in the case of ZnSe this agreement extends up to ∼600 meV. Such conclusion was drawn from Fig. 45 in Sec. XVIII of Supplemental Material [29]. That section contains also a more detailed discussion on the relation of our results for momentum relaxation times and scattering times and the results of Refs. [67] and [13].

Comparison of the momentum relaxation times for calculations with PBE and HSE06 functional gives as an additional insight why the HSE06 calculation gives lower values of mobility. As already discussed, the HSE06 calculation yields a higher effective mass than PBE calculation. It is not obvious whether a higher effective mass would lead to larger or smaller momentum relaxation times, because two opposing effects stemming from effective mass lead to the change of momentum relaxation time. On the one hand, larger effective mass leads to smaller phase space for scattering, which would lead to increased momentum relaxation time. On the other hand, for larger effective mass, the phonon momenta involved in the scattering event are smaller on average (when electron energy is sufficiently large that LO phonon emission is possible), the scattering matrix element is therefore larger, which would lead to decreased momentum relaxation time. In addition, HSE scattering matrix elements are larger because of smaller dielectric constant, which would lead to decreased momentum relaxation time. The results shown in Fig. 10 and in Figs. 42–44 in Supplemental Material [29] suggest that the effects that tend to decrease the momentum relaxation time prevail so that the momentum relaxation time is smaller in HSE06 calculation when the effective mass is larger. Larger effective mass also yields smaller band velocities. Therefore, given the fact that both the momentum relaxation times and the band velocities are smaller for larger effective mass, the mobility is also smaller for larger effective mass. These results confirm the well-known fact that small effective masses are desirable to have large mobility.

Next possible simplification in the evaluation of the mobility could be to even avoid the electronic structure and phonon band structure calculation and assume a parabolic band structure, a dispersionless phonon mode and Fröhlich coupling between electrons and phonons. This is a textbook model of electrons, phonons, and their coupling in polar semiconductors. The results obtained within such a model are shown as well in Fig. 8 (labeled as "Fröhlich parab."). These results differ very little from the previous model (where full electronic and LO phonon dispersions are considered), suggesting that these are a viable alternative for mobility calculation at higher temperatures.

However, if one is interested to obtain reasonably accurate results for phonon-limited mobility at lower temperatures, the approach where only the LO phonon mode is considered is clearly not appropriate. To obtain a simpler model, which could be accurate in the broader range of temperatures, we consider the possibility of including only the short-ranged or the long-ranged term in Eq. (18) in Supplemental Material [29] for electron-phonon scattering elements. The results

obtained when only the short-ranged term is included are presented in Fig. 8 (labeled as "SR"), while the results obtained when only the long-ranged term is included fully coincide with the full mobility result (labeled as "all modes"). We therefore conclude that the long-ranged part of electron-phonon interaction fully determines the mobility, while it can be evaluated directly from Eq. (17) in Supplemental Material [29] without the need to previously obtain electron-phonon coupling constants from DFPT and without the need to perform their interpolation.

IV. CONCLUSION

We conclude by pointing out several lessons learned from our *ab initio* calculations of electron mobility in representative II-VI semiconductors. Our study points to the necessity of having accurate band structure and dielectric constants as input to the calculation. For example, in the case of ZnSe one obtains twofold larger mobility at room temperature if the values obtained from PBE are directly used. While previous studies of other materials have also considered the issue of band structure and dielectric constants accuracy, the changes of mobility when local density approximation (LDA) or PBE results were replaced by more accurate results were relatively small (around 15% in the case of silicon in Ref. [9] and around 25% in the case of GaAs in Ref. [8]).

Since the whole approach that includes the interpolation of electron-phonon coupling constants to a dense grid is rather computationally demanding, we used the results obtained to benchmark possible simpler models that should yield comparable accuracy. Such models have the potential to be used in high-throughput screening of materials with desirable properties, where fast calculation of material properties in the screening process is needed.

We found that the Fröhlich model of electron-phonon coupling constants can give reasonably accurate results at temperatures around room temperature for these direct band gap materials where all relevant electronic states are at the vicinity of the Γ point and no intervalley scattering effects are present. Additional simplification of such model where parabolic bands are assumed gives essentially the same results. These two results stem from the fact that the band structure of the materials considered in the relevant range of energies at the bottom of the conduction band is nearly isotropic.

We also found that the long-ranged part of the electron-phonon interaction fully determines the mobility. Therefore, the approach where only this part is calculated is a viable alternative that avoids the need to perform interpolation of electron-phonon coupling constants.

ACKNOWLEDGMENTS

The author acknowledges funding provided by the Institute of Physics Belgrade, through the grant by Ministry of Education, Science and Technological Development of the Republic of Serbia. Numerical simulations were run on the PARADOX-IV supercomputing facility at the Scientific Computing Laboratory, National Center of Excellence for the Study of Complex Systems, Institute of Physics Belgrade.

[1] P. Hohenberg and W. Kohn, Inhomogeneous electron gas, Phys. Rev. **136**, B864 (1964).
[2] W. Kohn and L. J. Sham, Self-consistent equations including exchange and correlation effects, Phys. Rev. **140**, A1133 (1965).
[3] M. C. Payne, M. P. Teter, D. C. Allan, T. A. Arias, and J. D. Joannopoulos, Iterative minimization techniques for ab initio total-energy calculations: Molecular dynamics and conjugate gradients, Rev. Mod. Phys. **64**, 1045 (1992).
[4] S. Baroni, S. de Gironcoli, A. Dal Corso, and P. Giannozzi, Phonons and related crystal properties from density-functional perturbation theory, Rev. Mod. Phys. **73**, 515 (2001).
[5] X. Gonze and C. Lee, Dynamical matrices, Born effective charges, dielectric permittivity tensors, and interatomic force constants from density-functional perturbation theory, Phys. Rev. B **55**, 10355 (1997).
[6] F. Giustino, M. L. Cohen, and S. G. Louie, Electron-phonon interaction using Wannier functions, Phys. Rev. B **76**, 165108 (2007).
[7] M. Fiorentini and N. Bonini, Thermoelectric coefficients of *n*-doped silicon from first principles via the solution of the Boltzmann transport equation, Phys. Rev. B **94**, 085204 (2016).
[8] J. Ma, A. S. Nissimagoudar, and W. Li, First-principles study of electron and hole mobilities of Si and GaAs, Phys. Rev. B **97**, 045201 (2018).
[9] S. Poncé, E. R. Margine, and F. Giustino, Towards predictive many-body calculations of phonon-limited carrier mobilities in semiconductors, Phys. Rev. B **97**, 121201(R) (2018).
[10] W. Li, Electrical transport limited by electron-phonon coupling from Boltzmann transport equation: An ab initio study of Si, Al, and MoS_2, Phys. Rev. B **92**, 075405 (2015).
[11] C. Verdi and F. Giustino, Fröhlich Electron-Phonon Vertex from First Principles, Phys. Rev. Lett. **115**, 176401 (2015).
[12] J. Sjakste, N. Vast, M. Calandra, and F. Mauri, Wannier interpolation of the electron-phonon matrix elements in polar semiconductors: Polar-optical coupling in GaAs, Phys. Rev. B **92**, 054307 (2015).
[13] J.-J. Zhou and M. Bernardi, *Ab initio* electron mobility and polar phonon scattering in GaAs, Phys. Rev. B **94**, 201201(R) (2016).
[14] T.-H. Liu, J. Zhou, B. Liao, D. J. Singh, and G. Chen, First-principles mode-by-mode analysis for electron-phonon scattering channels and mean free path spectra in GaAs, Phys. Rev. B **95**, 075206 (2017).
[15] S. Poncé, D. Jena, and F. Giustino, Hole mobility of strained GaN from first principles, Phys. Rev. B **100**, 085204 (2019).
[16] S. Poncé, D. Jena, and F. Giustino, Route to High Hole Mobility in GaN Via Reversal of Crystal-Field Splitting, Phys. Rev. Lett. **123**, 096602 (2019).
[17] F. Macheda and N. Bonini, Magnetotransport phenomena in *p*-doped diamond from first principles, Phys. Rev. B **98**, 201201(R) (2018).

[18] S. Poncé, M. Schlipf, and F. Giustino, Origin of low carrier mobilities in halide perovskites, ACS Energy Lett. **4**, 456 (2019).

[19] J. Ma, Y. Chen, and W. Li, Intrinsic phonon-limited charge carrier mobilities in thermoelectric SnSe, Phys. Rev. B **97**, 205207 (2018).

[20] F. Meng, J. Ma, J. He, and W. Li, Phonon-limited carrier mobility and temperature-dependent scattering mechanism of 3*C*-SiC from first principles, Phys. Rev. B **99**, 045201 (2019).

[21] S. Poncé, W. Li, S. Reichardt, and F. Giustino, First-principles calculations of charge carrier mobility and conductivity in bulk semiconductors and two-dimensional materials, Rep. Prog. Phys. **83**, 036501 (2020).

[22] F. Murphy-Armando and S. Fahy, First-principles calculation of carrier-phonon scattering in *n*-type $Si_{1-x}Ge_x$ alloys, Phys. Rev. B **78**, 035202 (2008).

[23] D. Yu, Y. Zhang, and F. Liu, First-principles study of electronic properties of biaxially strained silicon: Effects on charge carrier mobility, Phys. Rev. B **78**, 245204 (2008).

[24] O. D. Restrepo, K. Varga, and S. T. Pantelides, First-principles calculations of electron mobilities in silicon: Phonon and Coulomb scattering, Appl. Phys. Lett. **94**, 212103 (2009).

[25] Z. Wang, S. Wang, S. Obukhov, N. Vast, J. Sjakste, V. Tyuterev, and N. Mingo, Thermoelectric transport properties of silicon: Toward an *ab initio* approach, Phys. Rev. B **83**, 205208 (2011).

[26] J. Cao, J. D. Querales-Flores, A. R. Murphy, S. Fahy, and I. Savić, Dominant electron-phonon scattering mechanisms in *n*-type PbTe from first principles, Phys. Rev. B **98**, 205202 (2018).

[27] S. Adachi, *Handbook on Physical Properties of Semiconductors, Volume 3, II-VI Compound Semiconductors* (Kluwer Academic Publishers, Boston, 2004).

[28] N. Marzari and D. Vanderbilt, Maximally localized generalized Wannier functions for composite energy bands, Phys. Rev. B **56**, 12847 (1997).

[29] See Supplemental Material at http://link.aps.org/supplemental/10.1103/PhysRevB.104.085203 for additional details.

[30] G. Brunin, H. P. C. Miranda, M. Giantomassi, M. Royo, M. Stengel, M. J. Verstraete, X. Gonze, G.-M. Rignanese, and G. Hautier, Electron-Phonon Beyond Fröhlich: Dynamical Quadrupoles in Polar and Covalent Solids, Phys. Rev. Lett. **125**, 136601 (2020).

[31] V. A. Jhalani, J.-J. Zhou, J. Park, C. E. Dreyer, and M. Bernardi, Piezoelectric Electron-Phonon Interaction from *Ab Initio* Dynamical Quadrupoles: Impact on Charge Transport in Wurtzite GaN, Phys. Rev. Lett. **125**, 136602 (2020).

[32] C. Jacoboni, *Theory of Electron Transport in Semiconductors* (Springer, Berlin, 2010).

[33] J. P. Perdew, K. Burke, and M. Ernzerhof, Generalized Gradient Approximation Made Simple, Phys. Rev. Lett. **77**, 3865 (1996).

[34] J. Heyd, G. E. Scuseria, and M. Ernzerhof, Hybrid functionals based on a screened Coulomb potential, J. Chem. Phys. **118**, 8207 (2003).

[35] A. V. Krukau, O. A. Vydrov, A. F. Izmaylov, and G. E. Scuseria, Influence of the exchange screening parameter on the performance of screened hybrid functionals, J. Chem. Phys. **125**, 224106 (2006).

[36] X. Gonze, B. Amadon, P.-M. Anglade, J.-M. Beuken, F. Bottin, P. Boulanger, F. Bruneval, D. Caliste, R. Caracas, M. Côté, T. Deutsch, L. Genovese, P. Ghosez, M. Giantomassi, S. Goedecker, D. Hamann, P. Hermet, F. Jollet, G. Jomard, S. Leroux *et al.*, ABINIT: First-principles approach to material and nanosystem properties, Comput. Phys. Commun. **180**, 2582 (2009).

[37] X. Gonze, F. Jollet, F. Abreu Araujo, D. Adams, B. Amadon, T. Applencourt, C. Audouze, J.-M. Beuken, J. Bieder, A. Bokhanchuk, E. Bousquet, F. Bruneval, D. Caliste, M. Côté, F. Dahm, F. Da Pieve, M. Delaveau, M. Di Gennaro, B. Dorado, C. Espejo *et al.*, Recent developments in the ABINIT software package, Comput. Phys. Commun. **205**, 106 (2016).

[38] D. R. Hamann, Optimized norm-conserving Vanderbilt pseudopotentials, Phys. Rev. B **88**, 085117 (2013).

[39] M. van Setten, M. Giantomassi, E. Bousquet, M. Verstraete, D. Hamann, X. Gonze, and G.-M. Rignanese, The PseudoDojo: Training and grading a 85 element optimized norm-conserving pseudopotential table, Comput. Phys. Commun. **226**, 39 (2018).

[40] O. Madelung, *Semiconductors: Data Handbook*, 3rd ed. (Springer, Berlin, 2004).

[41] I. Souza, N. Marzari, and D. Vanderbilt, Maximally localized Wannier functions for entangled energy bands, Phys. Rev. B **65**, 035109 (2001).

[42] A. A. Mostofi, J. R. Yates, G. Pizzi, Y.-S. Lee, I. Souza, D. Vanderbilt, and N. Marzari, An updated version of wannier90: A tool for obtaining maximally-localised wannier functions, Comput. Phys. Commun. **185**, 2309 (2014).

[43] J. P. Perdew, Density functional theory and the band gap problem, Int. J. Quantum Chem. **28**, 497 (1985).

[44] A. J. Garza and G. E. Scuseria, Predicting band gaps with hybrid density functionals, J. Phys. Chem. Lett. **7**, 4165 (2016).

[45] L. C. Lew Yan Voon and M. Willatzen, *The k·p Method: Electronic Properties of Semiconductors* (Springer-Verlag, Berlin, 2009).

[46] Z. Chen, J. Sjakste, J. Dong, A. Taleb-Ibrahimi, J.-P. Rueff, A. Shukla, J. Peretti, E. Papalazarou, M. Marsi, and L. Perfetti, Ultrafast dynamics of hot carriers in a quasi–two-dimensional electron gas on InSe, Proc. Natl. Acad. Sci. U.S.A. **117**, 21962 (2020).

[47] T. Sohier, M. Gibertini, and M. J. Verstraete, Remote free-carrier screening to boost the mobility of Fröhlich-limited two-dimensional semiconductors, Phys. Rev. Materials **5**, 024004 (2021).

[48] R. W. Nunes and X. Gonze, Berry-phase treatment of the homogeneous electric field perturbation in insulators, Phys. Rev. B **63**, 155107 (2001).

[49] I. Souza, J. Íñiguez, and D. Vanderbilt, First-Principles Approach to Insulators in Finite Electric Fields, Phys. Rev. Lett. **89**, 117602 (2002).

[50] O. Jepson and O. Anderson, The electronic structure of h.c.p. Ytterbium, Solid State Commun. **9**, 1763 (1971).

[51] M. Kawamura, Y. Gohda, and S. Tsuneyuki, Improved tetrahedron method for the Brillouin-zone integration applicable to response functions, Phys. Rev. B **89**, 094515 (2014).

[52] T. Yao, Characterization of ZnSe grown by molecular-beam epitaxy, J. Cryst. Growth **72**, 31 (1985).

[53] O. V. Emelyanenko, G. N. Ivanova, T. S. Lagunova, D. D. Nedeoglo, G. M. Shmelev, and A. V. Simashkevich, Scattering mechanisms of electrons in ZnSe crystals with high mobility, Phys. Status Solidi B **96**, 823 (1979).

[54] M. Aven and B. Segall, Carrier mobility and shallow impurity states in ZnSe and ZnTe, Phys. Rev. **130**, 81 (1963).
[55] G. Jones and J. Woods, The electrical properties of zinc selenide, J. Phys. D: Appl. Phys. **9**, 799 (1976).
[56] T. Marshall and J. Gaines, Impurity-band transport near the metal-insulator transition in ZnSe epilayers grown by molecular beam epitaxy, Appl. Phys. Lett. **56**, 2669 (1990).
[57] B. J. Skromme, S. M. Shibli, J. L. de Miguel, and M. C. Tamargo, Photoluminescence characterization of ZnSe doped with Ga by bulk and planar doping techniques in molecular-beam epitaxy, J. Appl. Phys. **65**, 3999 (1989).
[58] M. Aven, High electron mobility in zinc selenide through low-temperature annealing, J. Appl. Phys. **42**, 1204 (1971).
[59] B. Segall, M. R. Lorenz, and R. E. Halsted, Electrical properties of *n*-type CdTe, Phys. Rev. **129**, 2471 (1963).
[60] M. Nagabhooshanam and V. H. Babu, Mobility analysis in plastically deformed CdTe single crystals, J. Mater. Sci. **20**, 4329 (1985).
[61] K. Suzuki, S. Seto, T. Sawada, and K. Imai, Carrier transport properties of HPB CdZnTe and THM CdTe:Cl, IEEE Trans. Nucl. Sci. **49**, 1287 (2002).
[62] P. J. Sellin, A. W. Davies, A. Lohstroh, M. E. Ozsan, and J. Parkin, Drift mobility and mobility-lifetime products in CdTe:Cl grown by the travelling heater method, IEEE Trans. Nucl. Sci. **52**, 3074 (2005).
[63] J. H. Chang, T. Takai, B. H. Koo, J. S. Song, T. Handa, and T. Yao, Aluminum-doped *n*-type ZnTe layers grown by molecular-beam epitaxy, Appl. Phys. Lett. **79**, 785 (2001).
[64] R. A. Btirmeister Jr. and D. A. Stevenson, Electrical properties of *n*-type CdSe, Phys. Status Solidi B **24**, 683 (1967).
[65] F. Smith, High temperature electrical properties of CdSe: Evidence for a native donor, Solid State Commun. **8**, 263 (1970).
[66] D. L. Rode, Electron mobility in II-VI semiconductors, Phys. Rev. B **2**, 4036 (1970).
[67] V. A. Jhalani, J.-J. Zhou, and M. Bernardi, Ultrafast hot carrier dynamics in GaN and its impact on the efficiency droop, Nano Lett. **17**, 5012 (2017).

Supplemental material for: Calculations of electron mobility in II-VI semiconductors

Nenad Vukmirović*
Institute of Physics Belgrade, University of Belgrade, Pregrevica 118, 11080 Belgrade, Serbia

* nenad.vukmirovic@ipb.ac.rs

I. RELEVANT EQUATIONS

A. Electronic states and Wannier functions

Density functional theory is used to obtain the wave functions of electronic states $|\psi_{n\mathbf{k}}\rangle$ and the corresponding energies $\varepsilon_{n\mathbf{k}}$ which satisfy the eigenproblem of the Kohn-Sham single-particle Hamiltonian

$$H_{KS}\,|\psi_{n\mathbf{k}}\rangle = \varepsilon_{n\mathbf{k}}\,|\psi_{n\mathbf{k}}\rangle\,. \tag{1}$$

The index n denotes the electronic band, while $\mathbf{k}$ is the electronic wave vector from the first Brillouin zone.

Wannier functions are related to the wave functions of electronic states $|\psi_{n\mathbf{k}}\rangle$ as [1]

$$|w_{m\mathbf{R}}\rangle = \frac{1}{\sqrt{N_k}}\sum_{\mathbf{k}} e^{-\mathrm{i}\mathbf{k}\cdot\mathbf{R}}\sum_{n} U_{nm}(\mathbf{k})\,|\psi_{n\mathbf{k}}\rangle\,. \tag{2}$$

In previous equation, the index m denotes the Wannier functions (it is in the range $[1,\ldots,n_w]$ with n_w being the total number of constructed Wannier functions per unit cell), $\mathbf{R}$ is the direct lattice vector of the unit cell where the Wannier function is localized, while the summation is performed over the N_k electronic wave vectors $\mathbf{k}$ from the grid used to perform density functional theory calculation of the states $|\psi_{n\mathbf{k}}\rangle$. The matrices $U_{nm}(\mathbf{k})$ are unitary matrices of the transformation from the basis of Bloch states $|\psi_{n\mathbf{k}}\rangle$ to Wannier functions $|w_{m\mathbf{R}}\rangle$.

The matrix elements of the Kohn-Sham Hamiltonian in the Wannier representation are then given as

$$\langle w_{m_1\mathbf{R}_1}|H_{KS}|w_{m_2\mathbf{R}_2}\rangle = \frac{1}{N_k}\sum_{\mathbf{k}} e^{\mathrm{i}\mathbf{k}\cdot(\mathbf{R}_1-\mathbf{R}_2)}\cdot\Big[U(\mathbf{k})^{\dagger}h_d(\mathbf{k})U(\mathbf{k})\Big]_{m_1m_2} \tag{3}$$

where $h_d(\mathbf{k})$ is a diagonal matrix that contains the eigenenergies $\varepsilon_{n\mathbf{k}}$. To obtain the eigenstates and eigenenergies of the Kohn-Sham Hamiltonian at $\mathbf{K}$ points which are not from the grid used in the DFT calculation, one forms the matrix

$$h_{m_1m_2}(\mathbf{K}) = \sum_{\mathbf{R}} e^{\mathrm{i}\mathbf{K}\cdot\mathbf{R}}\,\langle w_{m_1\mathbf{0}}|H_{KS}|w_{m_2\mathbf{R}}\rangle \tag{4}$$

and solves its eigenvalue problem. The eigenvalues $\tilde{\varepsilon}_{n\mathbf{K}}$ of this matrix are the eigenenergies of H_{KS} at $\mathbf{K}$, while the eigenstates of H_{KS} are given as

$$\left|\tilde{\psi}_{n\mathbf{K}}\right\rangle = \frac{1}{\sqrt{N_k}}\sum_{\mathbf{R}} e^{\mathrm{i}\mathbf{K}\cdot\mathbf{R}}\sum_{m}\tilde{U}^{*}_{nm}(\mathbf{K})\,|w_{m\mathbf{R}}\rangle\,. \tag{5}$$

where the matrix $\tilde{U}(\mathbf{K})$ is the adjoint matrix of the matrix whose columns contain the eigenvectors of $h(\mathbf{K})$, while the symbol * denotes complex conjugation.

B. Electron-lattice coupling constants

Density functional perturbation theory calculation is used to obtain the coupling constants on the coarse grid of $\mathbf{k}$ and $\mathbf{q}$ points

$$\langle\psi_{n_1,\mathbf{k}+\mathbf{q}}|\frac{\partial H_{KS}}{\partial u_{-\mathbf{q}S\alpha}}|\psi_{n_2\mathbf{k}}\rangle \tag{6}$$

that describe coupling between electronic states $|\psi_{n_1,\mathbf{k}+\mathbf{q}}\rangle$ and $|\psi_{n_2\mathbf{k}}\rangle$ caused by lattice displacement of atom S in direction α. These lattice displacements form a wave whose wave vector is $-\mathbf{q}$ and the relation

$$u_{-\mathbf{q}S\alpha} = \frac{1}{N_k}\sum_{\mathbf{R}} e^{-\mathrm{i}\mathbf{q}\cdot\mathbf{R}}u_{\mathbf{R}S\alpha} \tag{7}$$

holds, where $u_{\mathbf{R}S\alpha}$ is the real space displacement in direction α of atom S that is located in primitive cell whose position is specified by direct lattice vector $\mathbf{R}$. In polar materials where atoms carry Born effective charges, the change of potential created when atoms are displaced is long-ranged. Direct transformation of matrix elements from

Eq. (6) to local representation would however erase part of the information about this long-ranged part. For this reason, the operator in Eq. (6) is first divided into short-ranged and long-ranged part as

$$\frac{\partial H_{KS}}{\partial u_{-\mathbf{q}S\alpha}} = \frac{\partial H_{KS}^{(SR)}}{\partial u_{-\mathbf{q}S\alpha}} + \frac{\partial V^{(LR)}}{\partial u_{-\mathbf{q}S\alpha}}. \tag{8}$$

The long-ranged operator which exists due to the presence of Born charges is given as [2]

$$\frac{\partial V^{(LR)}}{\partial u_{-\mathbf{q}S\alpha}} = \frac{\mathrm{i}e_0}{\varepsilon_0 V} \sum_{\mathbf{G}\neq-\mathbf{q}} \frac{e^{-\frac{\sigma^2}{2}(\mathbf{q}+\mathbf{G})\cdot\hat{\varepsilon}_{r1}^{\infty}\cdot(\mathbf{q}+\mathbf{G})}}{(\mathbf{q}+\mathbf{G})\cdot\hat{\varepsilon}_{r1}^{\infty}\cdot(\mathbf{q}+\mathbf{G})} e^{\mathrm{i}(\mathbf{q}+\mathbf{G})(\mathbf{r}-\mathbf{r}_S)} \left[\hat{Z}_{1S}\cdot(\mathbf{q}+\mathbf{G})\right]_{\alpha}, \tag{9}$$

where e_0 is the elementary charge, ε_0 is the vacuum permittivity, V is the volume of the primitive cell of the crystal, $\hat{\varepsilon}_{r1}^{\infty}$ is the tensor of the high-frequency relative dielectric constant, $\hat{Z}_{1S}$ is the tensor of Born effective charge for atom S, $\mathbf{r}_S$ is the position of atom S in the primitive cell, while the summation is performed over reciprocal lattice vectors $\mathbf{G}$ that satisfy the condition $\mathbf{G}+\mathbf{q}\neq 0$ and σ is the parameter that controls the convergence of this sum. We note in passing that most recent studies [3, 4] have addressed the possibility of including additional quadrupole terms in Eq. (9). The matrix elements of the short-ranged part are next evaluated as

$$\langle\psi_{n_1,\mathbf{k}+\mathbf{q}}|\frac{\partial H_{KS}^{(SR)}}{\partial u_{-\mathbf{q}S\alpha}}|\psi_{n_2\mathbf{k}}\rangle = \langle\psi_{n_1,\mathbf{k}+\mathbf{q}}|\frac{\partial H_{KS}}{\partial u_{-\mathbf{q}S\alpha}}|\psi_{n_2\mathbf{k}}\rangle - \langle\psi_{n_1,\mathbf{k}+\mathbf{q}}|\frac{\partial V^{(LR)}}{\partial u_{-\mathbf{q}S\alpha}}|\psi_{n_2\mathbf{k}}\rangle\,. \tag{10}$$

To calculate $\langle\psi_{n_1,\mathbf{k}+\mathbf{q}}|\frac{\partial V^{(LR)}}{\partial u_{-\mathbf{q}S\alpha}}|\psi_{n_2\mathbf{k}}\rangle$ one needs to calculate the matrix elements $\langle\psi_{n_1,\mathbf{k}+\mathbf{q}}|e^{\mathrm{i}(\mathbf{q}+\mathbf{G})\cdot(\mathbf{r}-\mathbf{r}_S)}|\psi_{n_2\mathbf{k}}\rangle$. These are related to matrix elements between Wannier functions as

$$\langle\psi_{n_1,\mathbf{k}+\mathbf{q}}|e^{\mathrm{i}(\mathbf{q}+\mathbf{G})\cdot(\mathbf{r}-\mathbf{r}_S)}|\psi_{n_2\mathbf{k}}\rangle = \sum_{\mathbf{R}_e} e^{\mathrm{i}\mathbf{k}\cdot\mathbf{R}_e} \sum_{m_1m_2} U_{n_1m_1}(\mathbf{k}+\mathbf{q})\,\langle w_{m_1\mathbf{0}}|e^{\mathrm{i}(\mathbf{q}+\mathbf{G})\cdot(\mathbf{r}-\mathbf{r}_S)}|w_{m_2\mathbf{R}_e}\rangle \left[U(\mathbf{k})^{\dagger}\right]_{m_2n_2}. \tag{11}$$

To simplify Eq. (11) we further note that dominant terms in the sum in Eq. (9) are those with small values of $|\mathbf{q}+\mathbf{G}|$. For these terms, the $e^{\mathrm{i}(\mathbf{q}+\mathbf{G})\cdot(\mathbf{r}-\mathbf{r}_S)}$ factor in Eq. (11) is a slowly varying function of $\mathbf{r}$ on the length scale of Wannier function localization. Therefore, we can use the following approximation

$$\langle w_{m_1\mathbf{0}}|e^{\mathrm{i}(\mathbf{q}+\mathbf{G})\cdot(\mathbf{r}-\mathbf{r}_S)}|w_{m_2\mathbf{R}_e}\rangle \approx e^{\mathrm{i}(\mathbf{q}+\mathbf{G})\cdot\left(\mathbf{r}_{m_1}^{(w)}-\mathbf{r}_S\right)}\,\langle w_{m_1\mathbf{0}}|w_{m_2\mathbf{R}_e}\rangle = \delta_{m_1m_2}\delta_{\mathbf{R}_e,\mathbf{0}} e^{\mathrm{i}(\mathbf{q}+\mathbf{G})\cdot\left(\mathbf{r}_{m_1}^{(w)}-\mathbf{r}_S\right)}, \tag{12}$$

where $\mathbf{r}_{m_1}^{(w)}$ is the position of the center of the Wannier function $|w_{m_1\mathbf{0}}\rangle$. From Eqs. (11) and (12) it follows that

$$\langle\psi_{n_1,\mathbf{k}+\mathbf{q}}|e^{\mathrm{i}(\mathbf{q}+\mathbf{G})\cdot(\mathbf{r}-\mathbf{r}_S)}|\psi_{n_2\mathbf{k}}\rangle \approx \sum_{m} U_{n_1m}(\mathbf{k}+\mathbf{q}) e^{\mathrm{i}(\mathbf{q}+\mathbf{G})\cdot\left(\mathbf{r}_{m}^{(w)}-\mathbf{r}_S\right)} \left[U(\mathbf{k})^{\dagger}\right]_{mn_2}. \tag{13}$$

We note that Eq. (13) is different than corresponding equations in Refs. [5] and [2]. In Ref. [5] the approximations that lead to $\langle\psi_{n_1,\mathbf{k}+\mathbf{q}}|e^{\mathrm{i}(\mathbf{q}+\mathbf{G})\cdot(\mathbf{r}-\mathbf{r}_S)}|\psi_{n_2\mathbf{k}}\rangle \approx \delta_{n_1n_2}$ were used, while in Ref. [2] the approximations used lead to the expression

$$\langle\psi_{n_1,\mathbf{k}+\mathbf{q}}|e^{\mathrm{i}(\mathbf{q}+\mathbf{G})\cdot(\mathbf{r}-\mathbf{r}_S)}|\psi_{n_2\mathbf{k}}\rangle \approx \sum_{m} U_{n_1m}(\mathbf{k}+\mathbf{q}) \left[U(\mathbf{k})^{\dagger}\right]_{mn_2}. \tag{14}$$

Using a limited set of tests, we found that the final result for the mobility is essentially the same when Eq. (14) from Ref. [2] is used, while differences can be noticed if the approximation from Ref. [5] is used. The difference between electron-phonon coupling constants from different approaches occurs mainly for large phonon momenta and it is therefore not relevant for the present study.

Using Eqs. (2) and (7), matrix elements of the short-ranged part in Wannier representation can be expressed as

$$\langle w_{m_1\mathbf{0}}|\frac{\partial H_{KS}^{(SR)}}{\partial u_{\mathbf{R}_pS\alpha}}|w_{m_2\mathbf{R}_e}\rangle = \frac{1}{N_k^2}\sum_{\mathbf{kq}} e^{-\mathrm{i}\mathbf{k}\cdot\mathbf{R}_e} e^{-\mathrm{i}\mathbf{q}\cdot\mathbf{R}_p} \sum_{n_1n_2} \left[U(\mathbf{k}+\mathbf{q})^{\dagger}\right]_{m_1n_1} \langle\psi_{n_1,\mathbf{k}+\mathbf{q}}|\frac{\partial H_{KS}^{(SR)}}{\partial u_{-\mathbf{q}S\alpha}}|\psi_{n_2\mathbf{k}}\rangle\, U_{n_2m_2}(\mathbf{k}). \tag{15}$$

Using Eq. (5) one obtains the coupling elements due to short-ranged part between the Bloch states at arbitrary values of electron and phonon wave vector

$$\left\langle\tilde{\psi}_{n_1,\mathbf{K}+\mathbf{Q}}\right|\frac{\partial H_{KS}^{(SR)}}{\partial u_{-\mathbf{Q}S\alpha}}\left|\tilde{\psi}_{n_2\mathbf{K}}\right\rangle = \sum_{\mathbf{R}_e,\mathbf{R}_p} e^{\mathrm{i}\mathbf{K}\cdot\mathbf{R}_e} e^{\mathrm{i}\mathbf{Q}\cdot\mathbf{R}_p} \sum_{m_1m_2} \tilde{U}(\mathbf{K}+\mathbf{Q})_{n_1m_1}\,\langle w_{m_1\mathbf{0}}|\frac{\partial H_{KS}^{(SR)}}{\partial u_{\mathbf{R}_pS\alpha}}|w_{m_2\mathbf{R}_e}\rangle \left[\tilde{U}(\mathbf{K})^{\dagger}\right]_{m_2n_2}. \tag{16}$$

The coupling elements $\left\langle \tilde{\psi}_{n_1,\mathbf{K}+\mathbf{Q}} \middle| \frac{\partial V^{(LR)}}{\partial u_{-\mathbf{Q}S\alpha}} \middle| \tilde{\psi}_{n_2\mathbf{K}} \right\rangle$ due to long-ranged part for Bloch states at arbitrary values of electron and phonon wave vector can now be obtained using equations analogous to Eqs. (9), (11) and (13), where $\mathbf{k}$ and $\mathbf{q}$ are replaced by $\mathbf{K}$ and $\mathbf{Q}$, unitary matrices U are replaced by $\tilde{U}$ and Bloch states $|\psi_{n\mathbf{k}}\rangle$ are replaced by $\left|\tilde{\psi}_{n\mathbf{K}}\right\rangle$. For example, the equation analogous to Eq. (9) is

$$\frac{\partial V^{(LR)}}{\partial u_{-\mathbf{Q}S\alpha}} = \frac{\mathrm{i}e_0}{\varepsilon_0 V} \sum_{\mathbf{G}\neq-\mathbf{Q}} \frac{e^{-\frac{\sigma^2}{2}(\mathbf{Q}+\mathbf{G})\cdot\hat{\varepsilon}^{\infty}_{r2}\cdot(\mathbf{Q}+\mathbf{G})}}{(\mathbf{Q}+\mathbf{G})\cdot\hat{\varepsilon}^{\infty}_{r2}\cdot(\mathbf{Q}+\mathbf{G})} e^{\mathrm{i}(\mathbf{Q}+\mathbf{G})(\mathbf{r}-\mathbf{r}_S)} \left[\hat{Z}_{2S}\cdot(\mathbf{Q}+\mathbf{G})\right]_{\alpha}, \tag{17}$$

At this stage we also allow for the possibility to introduce the correction in the dielectric tensor or Born effective charges. Namely, if DFT calculation does not yield sufficiently accurate dielectric constant or Born effective charges and more accurate values are known (either from experiment or from the calculation using a more accurate method), we can use these more accurate values in the Eq. (17) to evaluate $\left\langle \tilde{\psi}_{n_1,\mathbf{K}+\mathbf{Q}} \middle| \frac{\partial V^{(LR)}}{\partial u_{-\mathbf{Q}S\alpha}} \middle| \tilde{\psi}_{n_2\mathbf{K}} \right\rangle$. This is emphasized in Eqs. (9) and (17) since the symbols $\hat{\varepsilon}^{\infty}_{r1}$ and $\hat{Z}_1$ are used in Eq. (9), while the symbols $\hat{\varepsilon}^{\infty}_{r2}$ and $\hat{Z}_2$ are used in Eq. (17).

With these elements at hand, the coupling elements for arbitrary $\mathbf{K}$ and $\mathbf{Q}$ are finally obtained as

$$\left\langle \tilde{\psi}_{n_1,\mathbf{K}+\mathbf{Q}} \middle| \frac{\partial H_{KS}}{\partial u_{-\mathbf{Q}S\alpha}} \middle| \tilde{\psi}_{n_2\mathbf{K}} \right\rangle = \left\langle \tilde{\psi}_{n_1,\mathbf{K}+\mathbf{Q}} \middle| \frac{\partial H^{(SR)}_{KS}}{\partial u_{-\mathbf{Q}S\alpha}} \middle| \tilde{\psi}_{n_2\mathbf{K}} \right\rangle + \left\langle \tilde{\psi}_{n_1,\mathbf{K}+\mathbf{Q}} \middle| \frac{\partial V^{(LR)}}{\partial u_{-\mathbf{Q}S\alpha}} \middle| \tilde{\psi}_{n_2\mathbf{K}} \right\rangle. \tag{18}$$

The electron-phonon coupling elements $\gamma^{\lambda}(\mathbf{K},\mathbf{Q})$ that enter the expression for momentum relaxation time are related to the coupling elements from Eq. (18) as

$$\gamma^{\lambda}(\mathbf{K},\mathbf{Q}) = \sum_{S\alpha} \sqrt{\frac{\hbar}{2M_S\omega_{\lambda\mathbf{Q}}}} \mathrm{e}(\mathbf{Q})^{\lambda}_{S\alpha} \left\langle \tilde{\psi}_{\mathbf{K}+\mathbf{Q}} \middle| \frac{\partial H_{KS}}{\partial u_{-\mathbf{Q}S\alpha}} \middle| \tilde{\psi}_{\mathbf{K}} \right\rangle, \tag{19}$$

where M_S is the mass of atom S, while $\mathrm{e}(\mathbf{Q})^{\lambda}_{S\alpha}$ are the components of the eigenvectors of the dynamical matrix

$$\sum_{T\beta} D(\mathbf{Q})_{S\alpha,T\beta} \mathrm{e}(\mathbf{Q})^{\lambda}_{T\beta} = \omega^2_{\lambda\mathbf{Q}} \mathrm{e}(\mathbf{Q})^{\lambda}_{S\alpha}. \tag{20}$$

II. ELECTRONIC BAND STRUCTURE INTERPOLATION

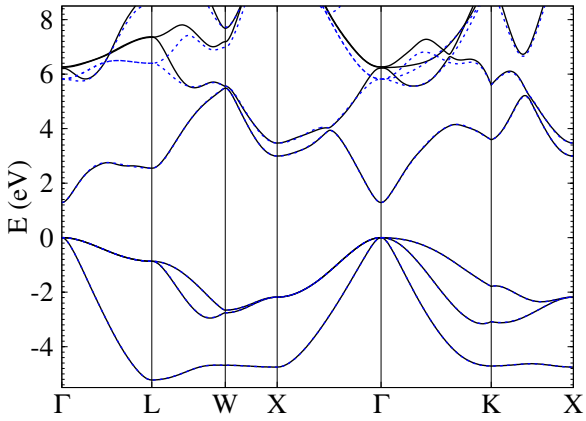

FIG. 1. Comparison of electronic band structure of ZnSe obtained using DFT calculation using the PBE functional (dashed line) and by its Wannier interpolation (full line).

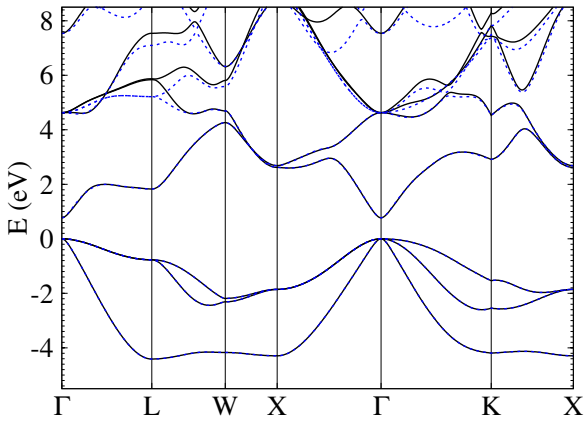

FIG. 2. Comparison of electronic band structure of CdTe obtained using DFT calculation using the PBE functional (dashed line) and by its Wannier interpolation (full line).

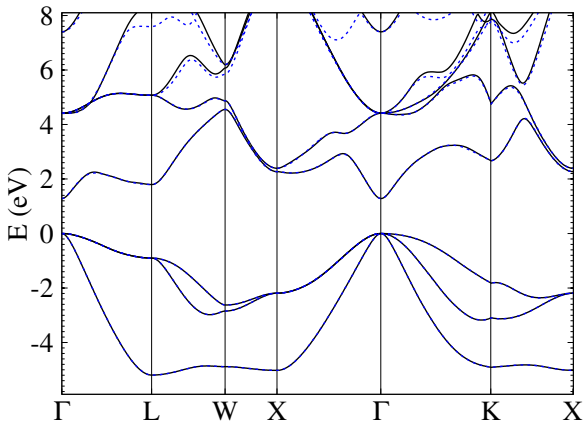

FIG. 3. Comparison of electronic band structure of ZnTe obtained using DFT calculation using the PBE functional (dashed line) and by its Wannier interpolation (full line).

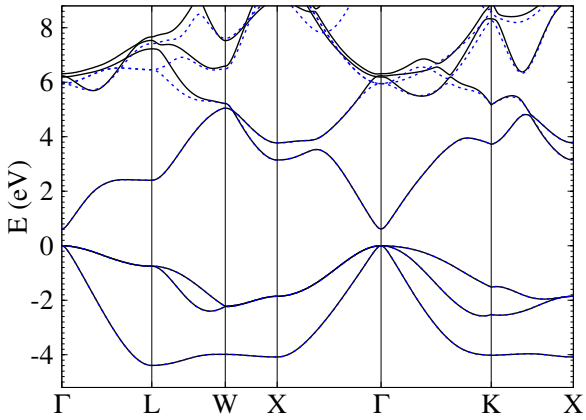

FIG. 4. Comparison of electronic band structure of CdSe obtained using DFT calculation using the PBE functional (dashed line) and by its Wannier interpolation (full line).

III. ELECTRONIC BAND STRUCTURE

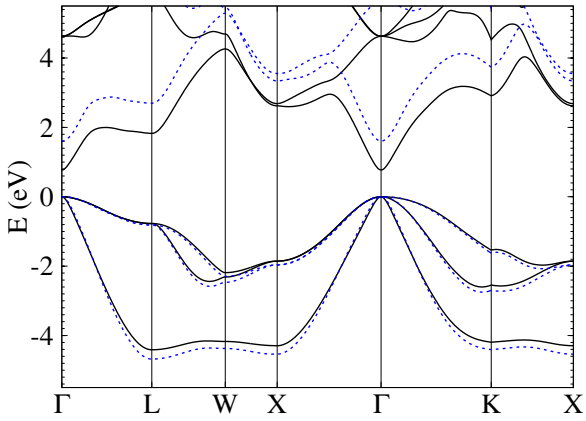

FIG. 5. Electronic band structure of CdTe calculated using the PBE functional (full line) and the hybrid HSE06 functional (dashed line).

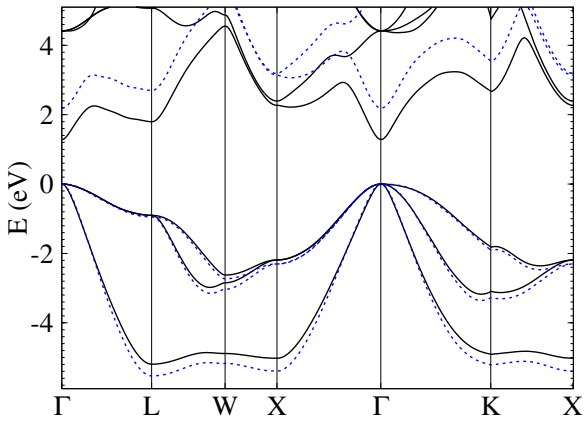

FIG. 6. Electronic band structure of ZnTe calculated using the PBE functional (full line) and the hybrid HSE06 functional (dashed line).

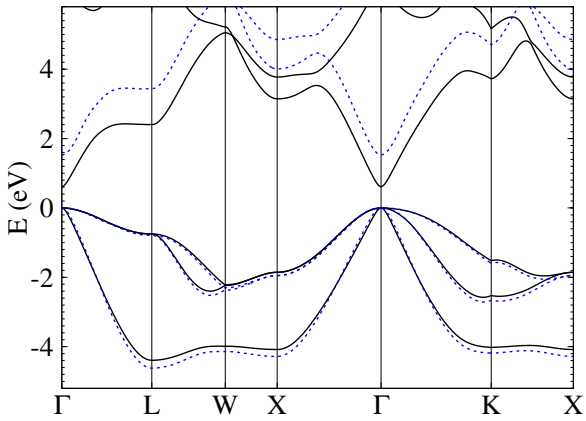

FIG. 7. Electronic band structure of CdSe calculated using the PBE functional (full line) and the hybrid HSE06 functional (dashed line).

IV. PHONON BAND STRUCTURE AND PHONON ENERGIES

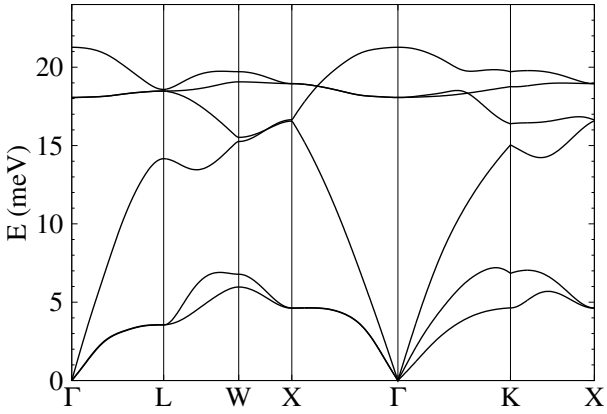

FIG. 8. Phonon band structure of CdTe.

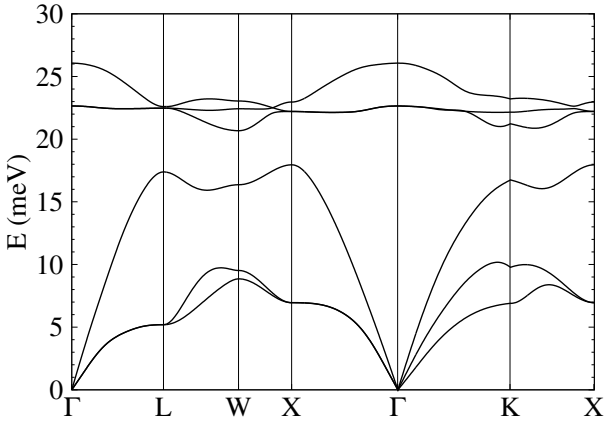

FIG. 9. Phonon band structure of ZnTe.

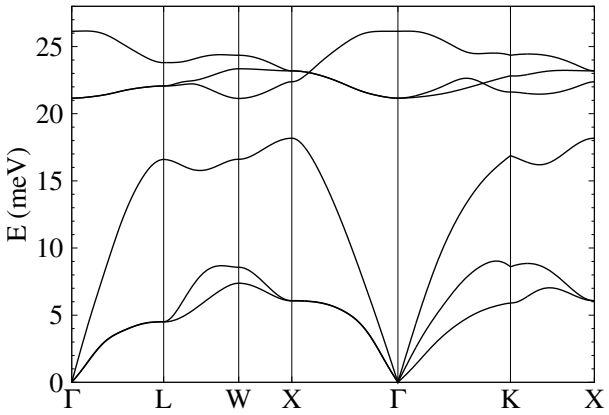

FIG. 10. Phonon band structure of CdSe.

		exp. (cm^{-1})	exp. (meV)	calc cor. (meV)	calc no cor. (meV)
Γ	TO	213	26.4	25.7	25.7
	LO	252	31.2	31.2	30.6
X	TA	71	8.8	9.2	8.1
	LA	193	23.9	24.2	23.9
	TO	220	27.3	26.2	26.4
	LO	213	26.4	25.1	24.7
L	TA	57	7.1	6.9	6.4
	LA	170	21.1	22.1	20.9
	TO	217	26.9	25.9	26.0
	LO	222	27.5	26.5	26.5

TABLE I. Phonon energies at characteristic points in the Brollouin zone for ZnSe. The label "exp." denotes the experimental results from Ref. [6], the label "calc cor." denotes the calculation where high-frequency dielectric constant was changed to the HSE06 value in the long-ranged part of the dynamical matrix, while the label "calc no cor." denotes the calculation where this correction was not performed.

		exp. (cm^{-1})	exp. (meV)	calc cor. (meV)	calc no cor. (meV)
Γ	TO	140	17.4	18.1	18.1
	LO	169	21.0	21.3	20.8
X	TA	35	4.3	4.6	3.4
	LA			16.6	16.3
	TO	148	18.3	18.9	19.2
	LO			16.6	16.3
L	TA	29	3.6	3.5	2.9
	LA	108	13.4	14.1	13.2
	TO	144	17.9	18.5	18.6
	LO	144	17.9	18.5	18.6

TABLE II. Phonon energies at characteristic points in the Brollouin zone for CdTe. The label "exp." denotes the experimental results from Ref. [6], the label "calc cor." denotes the calculation where high-frequency dielectric constant was changed to the HSE06 value in the long-ranged part of the dynamical matrix, while the label "calc no cor." denotes the calculation where this correction was not performed.

		exp. (cm^{-1})	exp. (meV)	calc cor. (meV)	calc no cor. (meV)
Γ	TO	177	21.9	22.6	22.7
	LO	207	25.7	26.1	25.6
X	TA	54	6.7	6.9	6.2
	LA	143	17.7	17.9	17.7
	TO	174	21.6	22.2	22.3
	LO	184	22.8	23.0	22.6
L	TA	42	5.2	5.2	4.9
	LA	135	16.7	17.4	16.7
	TO	173	21.4	22.5	22.4
	LO	180	22.3	22.6	22.6

TABLE III. Phonon energies at characteristic points in the Brollouin zone for ZnTe. The label "exp." denotes the experimental results from Ref. [6], the label "calc cor." denotes the calculation where high-frequency dielectric constant was changed to the HSE06 value in the long-ranged part of the dynamical matrix, while the label "calc no cor." denotes the calculation where this correction was not performed.

		exp. (cm^{-1})	exp. (meV)	calc cor. (meV)	calc no cor. (meV)
Γ	TO	169	21.0	21.2	21.3
	LO	211	26.2	26.1	25.4
X	TA			6.1	4.3
	LA			18.2	17.8
	TO			23.2	23.5
	LO			22.4	21.9
L	TA	34	4.2	4.5	3.6
	LA			16.6	15.3
	TO			22.1	22.3
	LO			23.8	23.7

TABLE IV. Phonon energies at characteristic points in the Brollouin zone for CdSe. The label "exp." denotes the experimental results from Ref. [6], the label "calc cor." denotes the calculation where high-frequency dielectric constant was changed to the HSE06 value in the long-ranged part of the dynamical matrix, while the label "calc no cor." denotes the calculation where this correction was not performed.

V. ELECTRON-PHONON COUPLING CONSTANTS

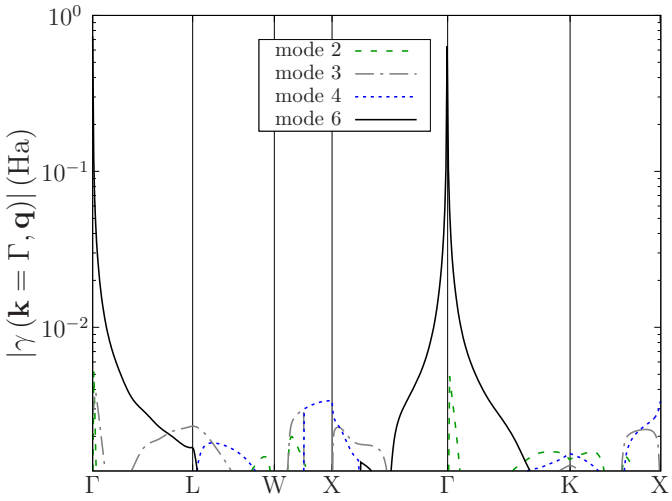

FIG. 11. Electron-phonon coupling constants for scattering of an electron at wave vector $\mathbf{k} = \Gamma$ with a phonon of a given mode at wave vector $\mathbf{q}$ in CdTe. The modes are labeled in ascending order of their energies at $\mathbf{q}$.

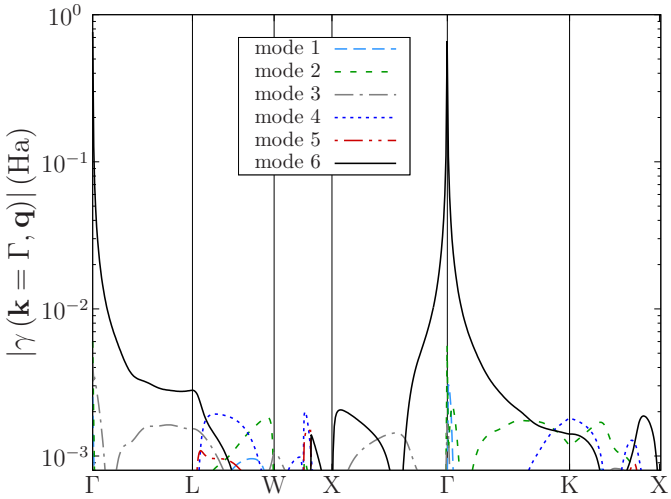

FIG. 12. Electron-phonon coupling constants for scattering of an electron at wave vector $\mathbf{k} = \Gamma$ with a phonon of a given mode at wave vector $\mathbf{q}$ in ZnTe. The modes are labeled in ascending order of their energies at $\mathbf{q}$.

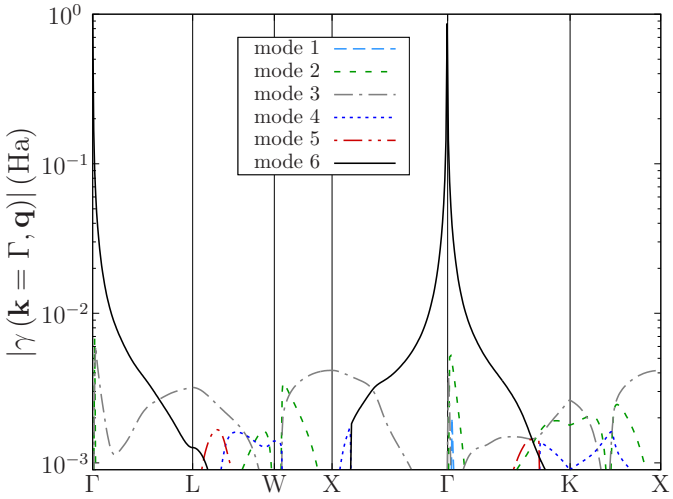

FIG. 13. Electron-phonon coupling constants for scattering of an electron at wave vector $\mathbf{k} = \Gamma$ with a phonon of a given mode at wave vector $\mathbf{q}$ in CdSe. The modes are labeled in ascending order of their energies at $\mathbf{q}$.

VI. ELECTRON-LATTICE COUPLING ELEMENTS

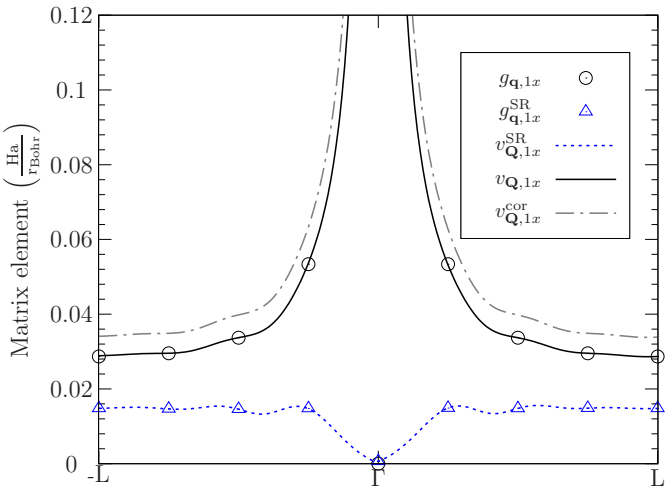

FIG. 14. Moduli of electron-lattice coupling elements in ZnSe: $g_{\mathbf{q},1x}$ denotes the element $\langle\psi_{n,\mathbf{k}+\mathbf{q}}|\frac{\partial H_{KS}}{\partial u_{-\mathbf{q}S\alpha}}|\psi_{n\mathbf{k}}\rangle$ for $\mathbf{k}=\Gamma$, S labels the first atom (Zn), $\alpha=x$, and n equal to the index of the conduction band; $g^{\text{SR}}_{\mathbf{q},1x}$ denotes the short-ranged part of the same element; $v^{\text{SR}}_{\mathbf{Q},1x}$ denotes $\left\langle\tilde{\psi}_{n,\mathbf{K}+\mathbf{Q}}\middle|\frac{\partial H^{(SR)}_{KS}}{\partial u_{-\mathbf{Q}S\alpha}}\middle|\tilde{\psi}_{n\mathbf{K}}\right\rangle$; $v_{\mathbf{Q},1x}$ denotes $\left\langle\tilde{\psi}_{n,\mathbf{K}+\mathbf{Q}}\middle|\frac{\partial H_{KS}}{\partial u_{-\mathbf{Q}S\alpha}}\middle|\tilde{\psi}_{n\mathbf{K}}\right\rangle$ when the long-ranged part was calculated using the PBE dielectric constant; $v^{\text{cor}}_{\mathbf{Q},1x}$ denotes the same element when the long-ranged part was calculated using the HSE06 dielectric constant

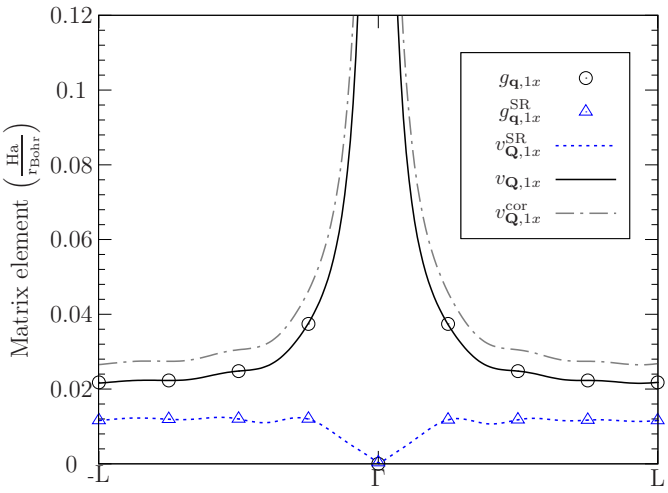

FIG. 15. Moduli of electron-lattice coupling elements in CdTe: $g_{\mathbf{q},1x}$ denotes the element $\langle\psi_{n,\mathbf{k}+\mathbf{q}}|\frac{\partial H_{KS}}{\partial u_{-\mathbf{q}S\alpha}}|\psi_{n\mathbf{k}}\rangle$ for $\mathbf{k}=\Gamma$, S labels the first atom (Cd), $\alpha=x$, and n equal to the index of the conduction band; $g^{\text{SR}}_{\mathbf{q},1x}$ denotes the short-ranged part of the same element; $v^{\text{SR}}_{\mathbf{Q},1x}$ denotes $\left\langle\tilde{\psi}_{n,\mathbf{K}+\mathbf{Q}}\middle|\frac{\partial H^{(SR)}_{KS}}{\partial u_{-\mathbf{Q}S\alpha}}\middle|\tilde{\psi}_{n\mathbf{K}}\right\rangle$; $v_{\mathbf{Q},1x}$ denotes $\left\langle\tilde{\psi}_{n,\mathbf{K}+\mathbf{Q}}\middle|\frac{\partial H_{KS}}{\partial u_{-\mathbf{Q}S\alpha}}\middle|\tilde{\psi}_{n\mathbf{K}}\right\rangle$ when the long-ranged part was calculated using the PBE dielectric constant; $v^{\text{cor}}_{\mathbf{Q},1x}$ denotes the same element when the long-ranged part was calculated using the HSE06 dielectric constant

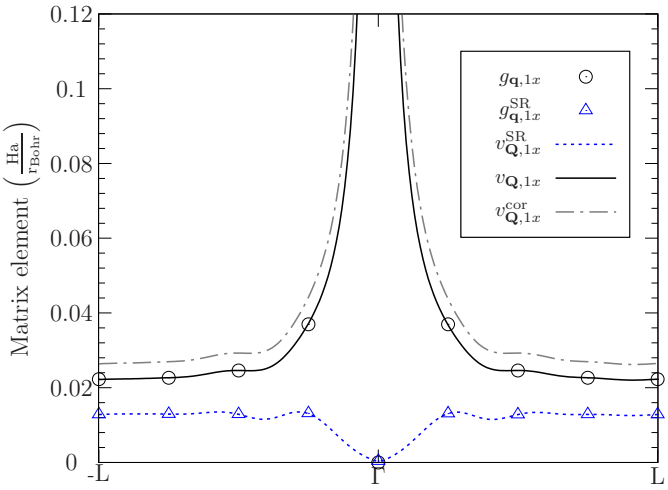

FIG. 16. Moduli of electron-lattice coupling elements in ZnTe: $g_{\mathbf{q},1x}$ denotes the element $\langle\psi_{n,\mathbf{k}+\mathbf{q}}|\frac{\partial H_{KS}}{\partial u_{-\mathbf{q}S\alpha}}|\psi_{n\mathbf{k}}\rangle$ for $\mathbf{k}=\Gamma$, S labels the first atom (Zn), $\alpha=x$, and n equal to the index of the conduction band; $g^{\text{SR}}_{\mathbf{q},1x}$ denotes the short-ranged part of the same element; $v^{\text{SR}}_{\mathbf{Q},1x}$ denotes $\left\langle\tilde{\psi}_{n,\mathbf{K}+\mathbf{Q}}\middle|\frac{\partial H^{(SR)}_{KS}}{\partial u_{-\mathbf{Q}S\alpha}}\middle|\tilde{\psi}_{n\mathbf{K}}\right\rangle$; $v_{\mathbf{Q},1x}$ denotes $\left\langle\tilde{\psi}_{n,\mathbf{K}+\mathbf{Q}}\middle|\frac{\partial H_{KS}}{\partial u_{-\mathbf{Q}S\alpha}}\middle|\tilde{\psi}_{n\mathbf{K}}\right\rangle$ when the long-ranged part was calculated using the PBE dielectric constant; $v^{\text{cor}}_{\mathbf{Q},1x}$ denotes the same element when the long-ranged part was calculated using the HSE06 dielectric constant

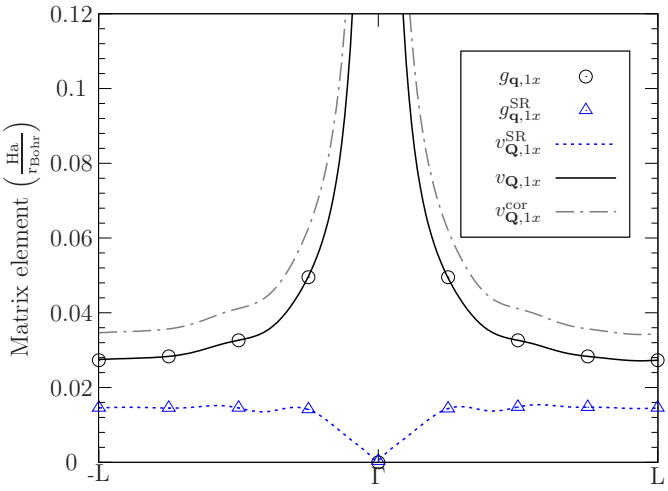

FIG. 17. Moduli of electron-lattice coupling elements in CdSe: $g_{\mathbf{q},1x}$ denotes the element $\langle\psi_{n,\mathbf{k}+\mathbf{q}}|\frac{\partial H_{KS}}{\partial u_{-\mathbf{q}S\alpha}}|\psi_{n\mathbf{k}}\rangle$ for $\mathbf{k}=\Gamma$, S labels the first atom (Cd), $\alpha=x$, and n equal to the index of the conduction band; $g^{\text{SR}}_{\mathbf{q},1x}$ denotes the short-ranged part of the same element; $v^{\text{SR}}_{\mathbf{Q},1x}$ denotes $\left\langle\tilde{\psi}_{n,\mathbf{K}+\mathbf{Q}}\middle|\frac{\partial H^{(SR)}_{KS}}{\partial u_{-\mathbf{Q}S\alpha}}\middle|\tilde{\psi}_{n\mathbf{K}}\right\rangle$; $v_{\mathbf{Q},1x}$ denotes $\left\langle\tilde{\psi}_{n,\mathbf{K}+\mathbf{Q}}\middle|\frac{\partial H_{KS}}{\partial u_{-\mathbf{Q}S\alpha}}\middle|\tilde{\psi}_{n\mathbf{K}}\right\rangle$ when the long-ranged part was calculated using the PBE dielectric constant; $v^{\text{cor}}_{\mathbf{Q},1x}$ denotes the same element when the long-ranged part was calculated using the HSE06 dielectric constant

VII. HIGH-FREQUENCY DIELECTRIC CONSTANTS AND BORN EFFECTIVE CHARGES

As mentioned in the main text, calculation of high-frequency dielectric constants and Born effective charges was performed using two different methods: (i) using density functional perturbation theory; (ii) by performing the calculation of polarization and atomic forces in finite electric field. The same plane-wave kinetic energy cut-off as in the case of band structure calculations was used since it was checked that it gives converged results for high-frequency dielectric constants and Born effective charges. In DFPT calculations we used the cubic grid in reciprocal space with spacing between nearest points of $\frac{2\pi}{N_g a_0}$, where a_0 is the lattice constant of the material and N_g is a positive integer. In finite electric-field calculations we used four-times-shifted Monkhorst Pack grid of size $N_g \times N_g \times N_g$. The dependence of dielectric constants obtained on N_g is presented in Figs. 18-21. We note that PBE calculations using two different methods converge towards the same value, as expected, while this convergence is slower in the case of finite electric field calculations. Due to computational limitations, it was not possible to perform hybrid functional calculations for large values of N_g. To obtain the value of dielectric constant within the hybrid functional approach we extrapolate the dependence of ε_r^∞ on N_g as follows. We note that the ratio of ε_r^∞ calculated in finite electric field calculations using the PBE and the hybrid functional approach is nearly the same for $N_g \in \{2, 4, 6\}$ where both calculations could be performed (this constant is 1.18 for ZnSe, 1.19 for ZnTe, 1.23 for CdTe and 1.26 for CdSe). Therefore we assume that this ratio will be the same for larger values of N_g as well and we obtain ε_r^∞ in hybrid functional approach as the converged value of PBE dielectric constant divided by the determined ratio.

Unlike dielectric constants, Born effective charges appear to be much less sensitive to the choice of functional and to the reciprocal space grid size. While the values of Born effective charge reported in the main text were obtained using formally the same procedure as for dielectric constants, its values would change very little if one simply took the $N_g = 6$ values in the calculation.

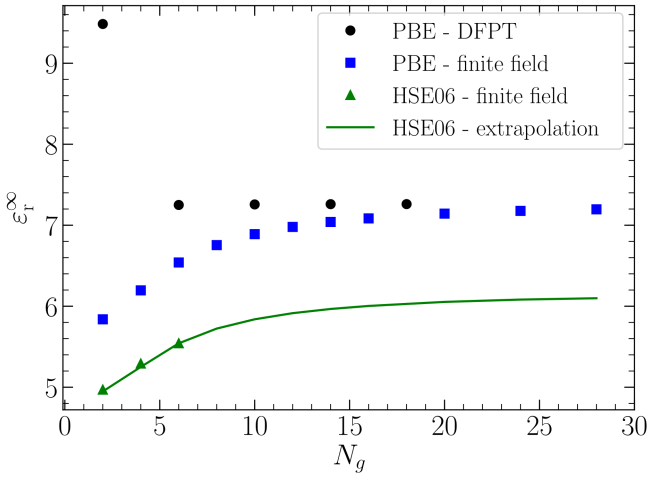

FIG. 18. Dependence of the calculated dielectric constant on the size of the grid in reciprocal space for the case of ZnSe.

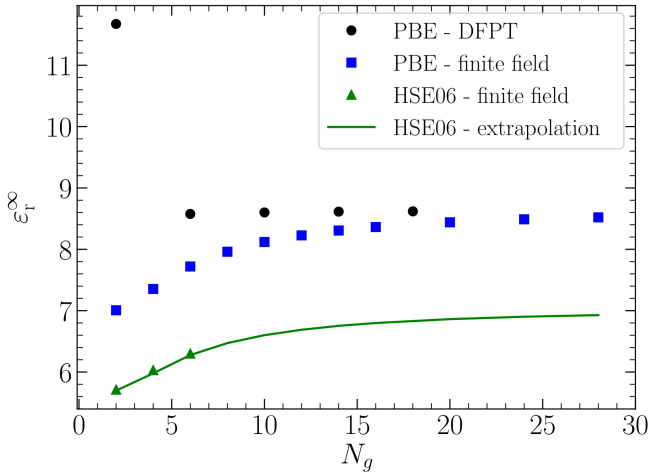

FIG. 19. Dependence of the calculated dielectric constant on the size of the grid in reciprocal space for the case of CdTe.

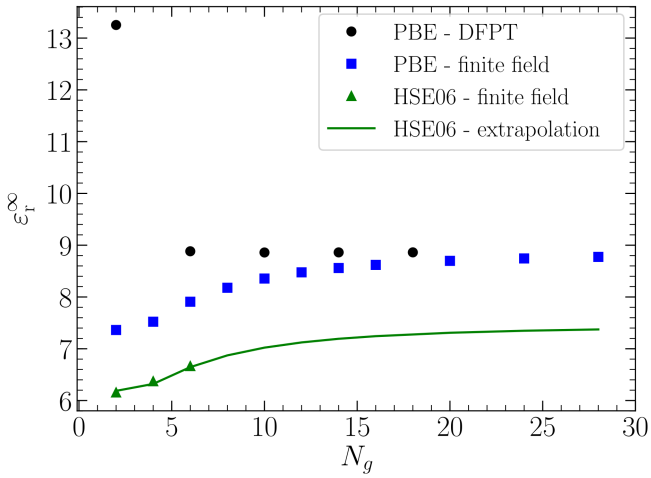

FIG. 20. Dependence of the calculated dielectric constant on the size of the grid in reciprocal space for the case of ZnTe.

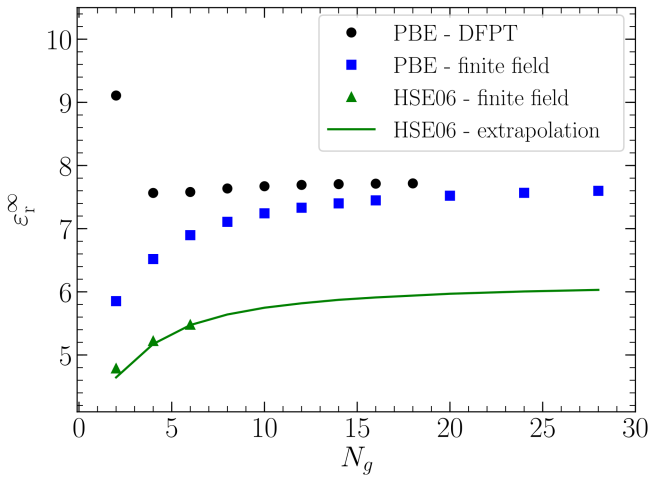

FIG. 21. Dependence of the calculated dielectric constant on the size of the grid in reciprocal space for the case of CdSe.

VIII. CONVERGENCE WITH RESPECT TO GRID SIZE

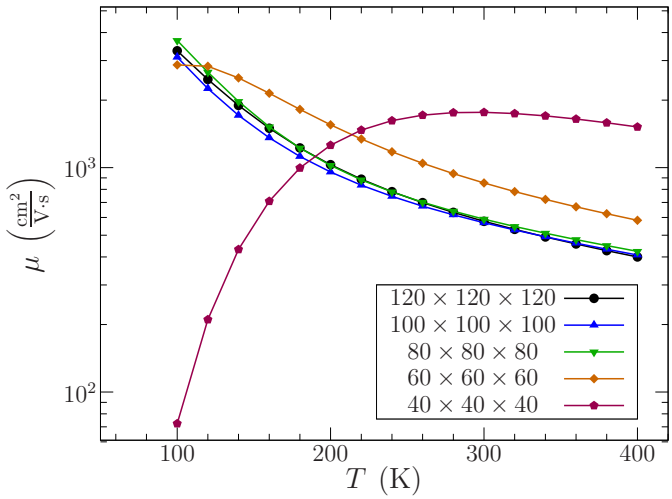

FIG. 22. Temperature dependence of mobility in ZnSe for different dense grid dimensions. The parameter ε_c was set to 140 meV in these calculations.

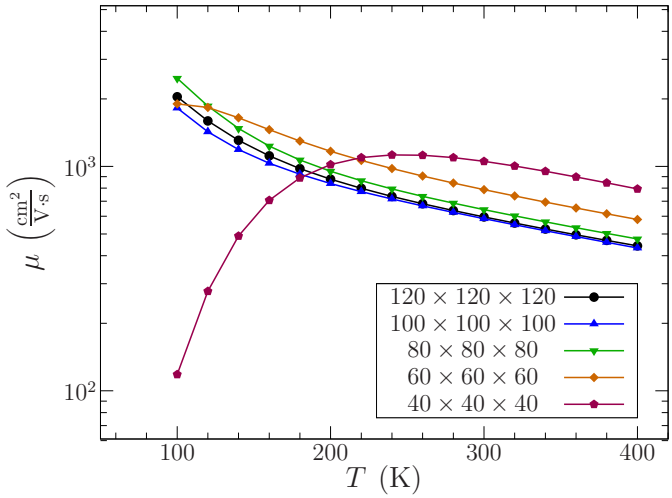

FIG. 23. Temperature dependence of mobility in CdTe for different dense grid dimensions. The parameter ε_c was set to 140 meV in these calculations.

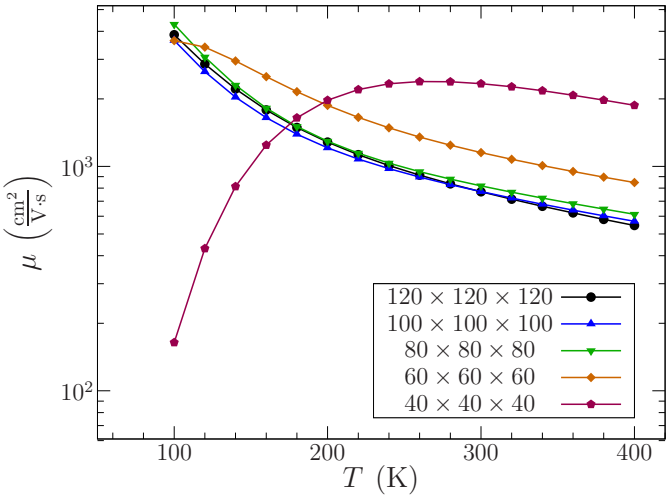

FIG. 24. Temperature dependence of mobility in ZnTe for different dense grid dimensions. The parameter ε_c was set to 140 meV in these calculations.

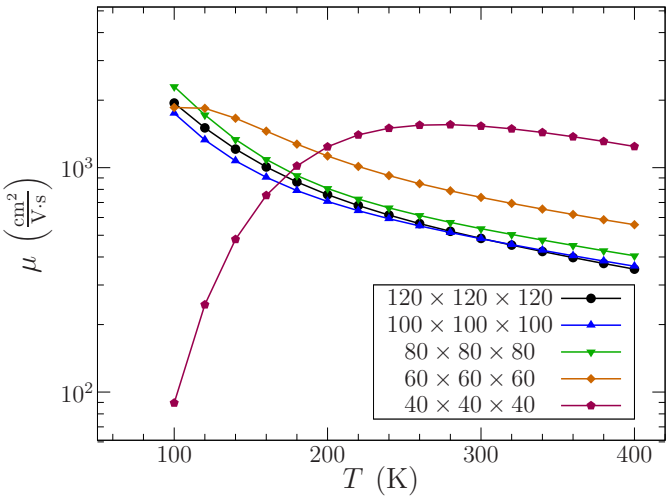

FIG. 25. Temperature dependence of mobility in CdSe for different dense grid dimensions. The parameter ε_c was set to 140 meV in these calculations.

IX. CONVERGENCE WITH RESPECT TO ε_c - THE ENERGY CUT-OFF THAT DETERMINES THE K POINTS USED IN THE CALCULATION

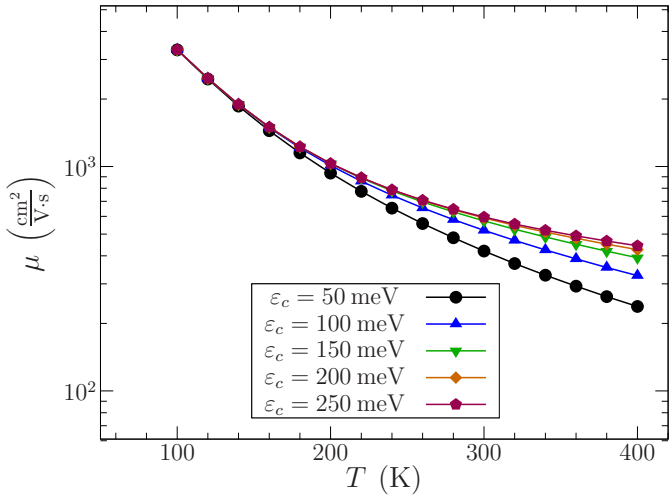

FIG. 26. Temperature dependence of mobility in ZnSe for different values of ε_c. The **K** point grid of size $120 \times 120 \times 120$ was used in these calculations.

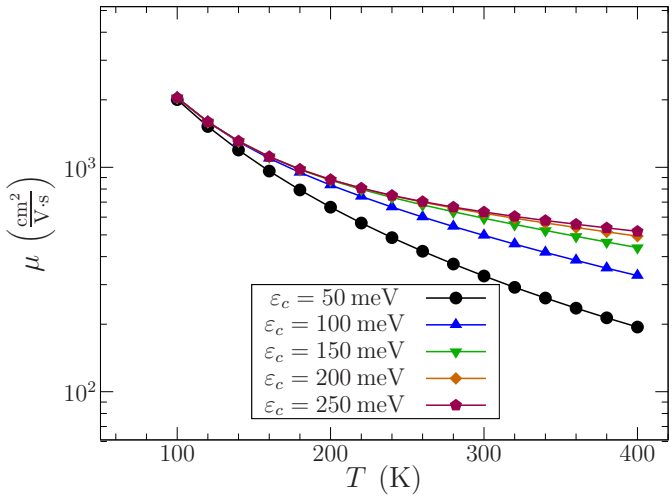

FIG. 27. Temperature dependence of mobility in CdTe for different values of ε_c. The **K** point grid of size $120 \times 120 \times 120$ was used in these calculations.

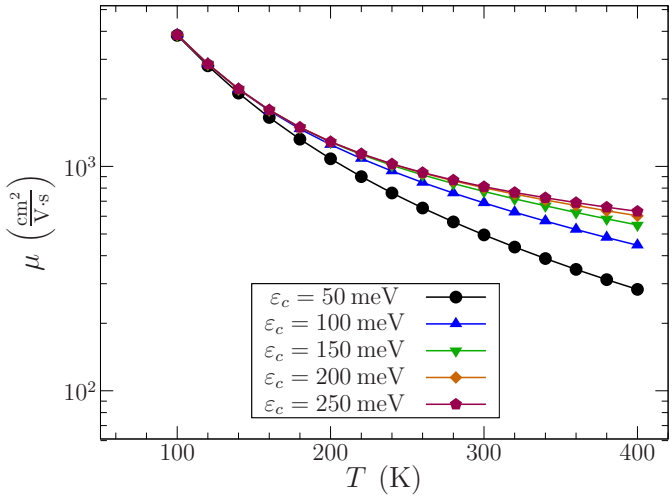

FIG. 28. Temperature dependence of mobility in ZnTe for different values of ε_c. The **K** point grid of size $120 \times 120 \times 120$ was used in these calculations.

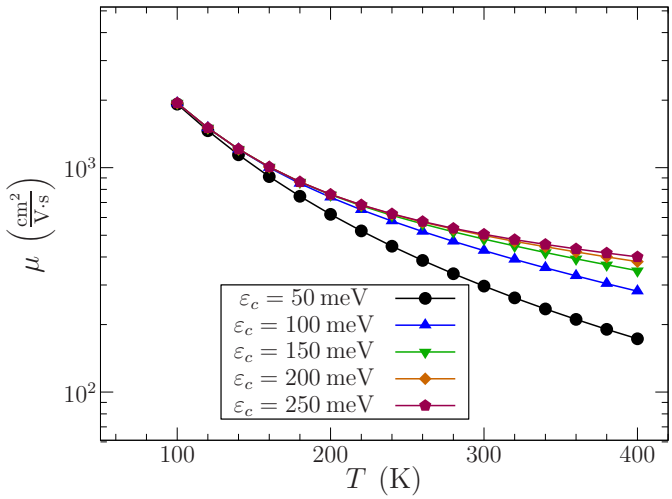

FIG. 29. Temperature dependence of mobility in CdSe for different values of ε_c. The **K** point grid of size $120 \times 120 \times 120$ was used in these calculations.

X. ACCURACY OF MOMENTUM RELAXATION TIME APPROXIMATION

All our calculations are based on momentum relaxation time approximation (MRTA) and in this section we estimate its accuracy. In the derivation of MRTA from Boltzmann equations one assumes at a certain point that

$$|\mathbf{v}_{\mathbf{k}}| \cdot \tau_{\mathbf{k}} \approx |\mathbf{v}_{\mathbf{k}'}| \cdot \tau_{\mathbf{k}'} \tag{21}$$

where $\mathbf{k}$ and $\mathbf{k}'$ are the wave vectors of the two states involved in the scattering event, $\tau_{\mathbf{k}}$ are the momentum relaxation times and $\mathbf{v}_{\mathbf{k}}$ are the band velocities. The approximation is best satisfied when the change of momentum in a scattering event is small. This is quite well satisfied for acoustic phonons which have low energies and therefore the two states $\mathbf{k}$ and $\mathbf{k}'$ need to have both similar energy and momenta to satisfy the conservation of energy and momentum in a scattering event. One could expect that the approximation could be less satisfactory in the case of optical phonons. For this reason, we investigate the effect of this approximation on mobility in a model with a single logitudinal optical phonon. We assume that the dispersion of the bands is parabolic and that the phonon is dispersionless. For such a model the Boltzmann equation can be solved with much smaller computational effort than in the general case, while the model has similar band dispersion and the main electron-phonon scattering mechanism as in the materials considered. For this reason, the conclusions on the validity of MRTA in this model could be extended to the materials considered. The comparison of the mobility obtained from the Boltzmann equation and from the MRTA is given in Figs. 30 and 31. The results indicate excellent accuracy of MRTA around room temperature. For all materials considered its accuracy (compared to the solution of Boltzmann equation) is better than 5% at room temperature, while the largest differences between the two models occur at lowest temperature of 100 K where they reach 30%. However, at the lowest temperatures the acoustic phonons, rather than longitudinal optical phonons, determine the electron-phonon scattering rate. One therefore expects better accuracy (than 30%) of MRTA applied to full model with all electron-phonon scattering mechanisms at lowest temperatures considered.

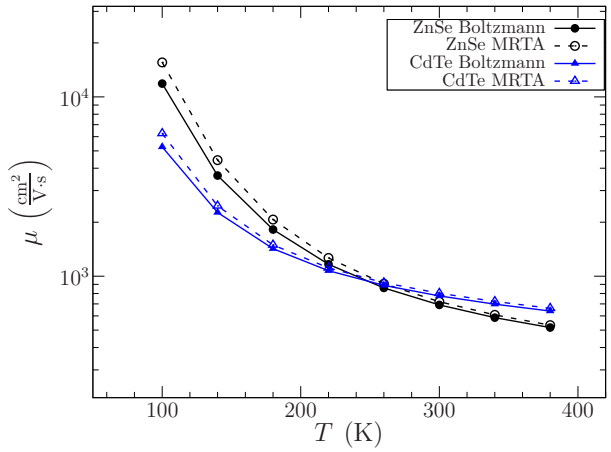

FIG. 30. Comparison of mobility for ZnSe and CdTe obtained from momentum relaxation time approximation (MRTA) and from the solution of Boltzmann equations in the case of of the model with parabolic bands and Fröhlich electron-phonon coupling with a single dispersionless phonon mode.

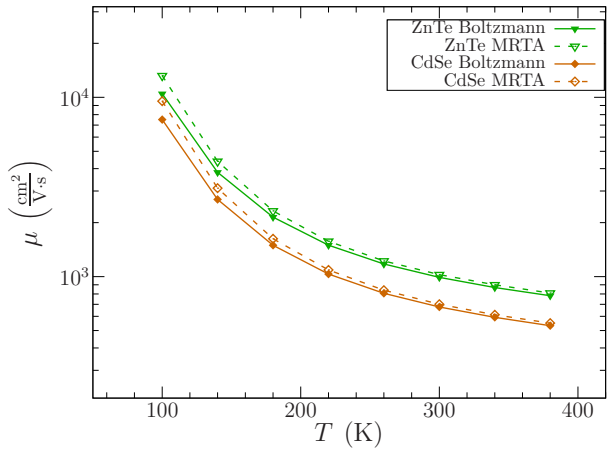

FIG. 31. Comparison of mobility for ZnTe and CdSe obtained from momentum relaxation time approximation (MRTA) and from the solution of Boltzmann equations in the case of of the model with parabolic bands and Fröhlich electron-phonon coupling with a single dispersionless phonon mode.

XI. COMPARISON OF THE EFFECTS OF BAND STRUCTURE CORRECTION AND DIELECTRIC CONSTANT CORRECTION ON THE MOBILITY

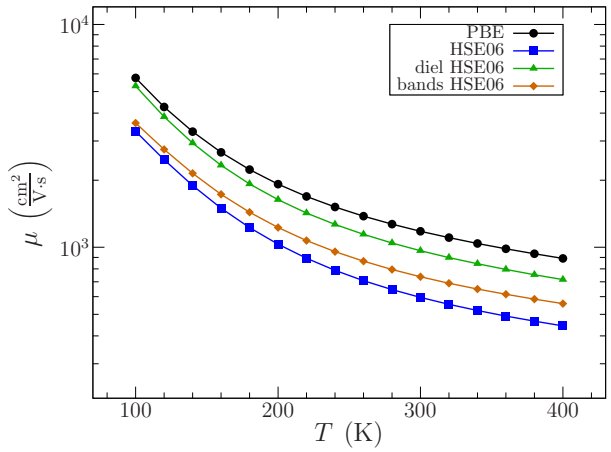

FIG. 32. Temperature dependence of mobility in ZnSe. The label PBE denotes the calculation where all quantities were calculated using the PBE functional, the label "diel HSE06" denotes the calculation where the dielectric constant obtained from the HSE06 functional was used, the label "bands HSE06" denotes the calculation where the band energies obtained from the HSE06 functional were used, while the label HSE06 denotes the calculation where the dielectric constant and band energies obtained from the HSE06 functional were used.

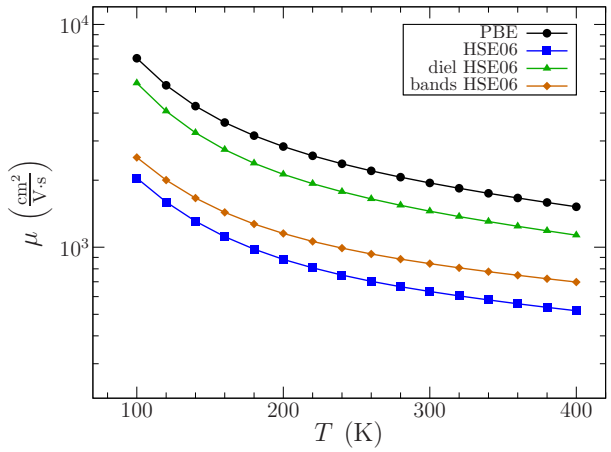

FIG. 33. Temperature dependence of mobility in CdTe. The label PBE denotes the calculation where all quantities were calculated using the PBE functional, the label "diel HSE06" denotes the calculation where the dielectric constant obtained from the HSE06 functional was used, the label "bands HSE06" denotes the calculation where the band energies obtained from the HSE06 functional were used, while the label HSE06 denotes the calculation where the dielectric constant and band energies obtained from the HSE06 functional were used.

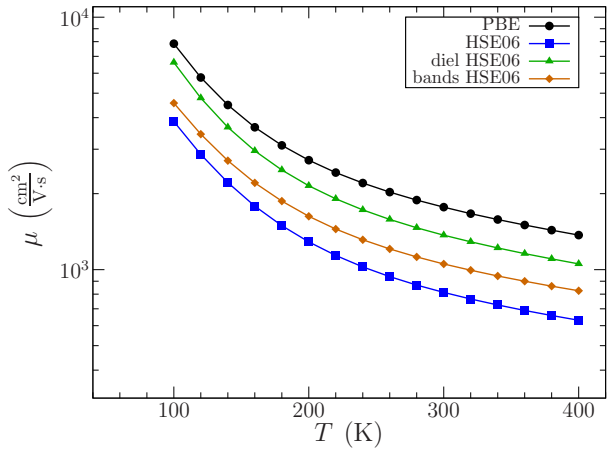

FIG. 34. Temperature dependence of mobility in ZnTe. The label PBE denotes the calculation where all quantities were calculated using the PBE functional, the label "diel HSE06" denotes the calculation where the dielectric constant obtained from the HSE06 functional was used, the label "bands HSE06" denotes the calculation where the band energies obtained from the HSE06 functional were used, while the label HSE06 denotes the calculation where the dielectric constant and band energies obtained from the HSE06 functional were used.

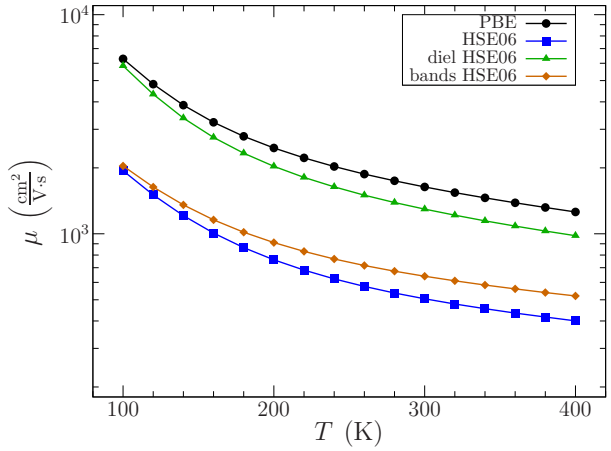

FIG. 35. Temperature dependence of mobility in CdSe. The label PBE denotes the calculation where all quantities were calculated using the PBE functional, the label "diel HSE06" denotes the calculation where the dielectric constant obtained from the HSE06 functional was used, the label "bands HSE06" denotes the calculation where the band energies obtained from the HSE06 functional were used, while the label HSE06 denotes the calculation where the dielectric constant and band energies obtained from the HSE06 functional were used.

XII. CALCULATED HALL FACTORS

The calculated values of electron Hall factors for the materials considered are given in Table V.

	ZnSe	ZnTe	CdSe	CdTe
100 K	1.12	1.12	1.08	1.07
200 K	1.14	1.09	1.05	1.04
300 K	1.06	1.05	1.05	1.07
400 K	1.05	1.05	1.08	1.10

TABLE V. Calculated values of electron Hall factors of investigated II-VI materials at different temperatures.

XIII. PARAMETERS USED IN THE FRÖHLICH MODEL

In Fröhlich model for electron-phonon interaction we use the following parameters that were taken from Ref. [6].

	ZnSe	ZnTe	CdSe	CdTe
ε_r^{∞}	5.9	6.9	6.2	7.1
$\varepsilon_r^{\mathrm{st}}$	8.9	9.4	9.6	10.4
$\hbar\omega_{\mathrm{LO}}$ (meV)	31.24	25.66	26.2	20.95

TABLE VI. The parameters of the Fröhlich model used in the calculation.

XIV. CONTRIBUTIONS OF DIFFERENT MODES TO MOBILITY AND THE MOBILITY OBTAINED FROM DIFFERENT MODELS

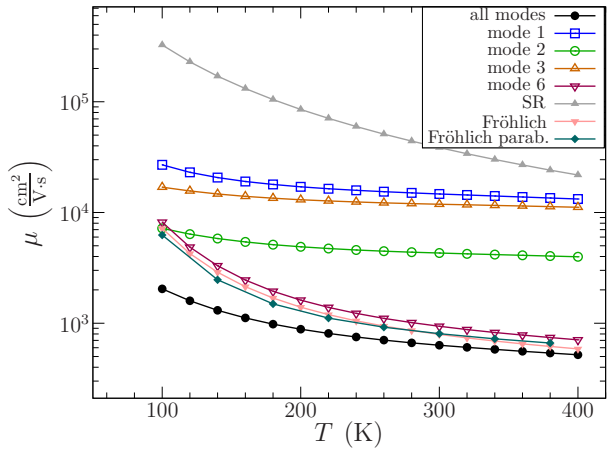

FIG. 36. Temperature dependence of mobility in CdTe: different contributions and the results from different models. The label "all modes" denotes the results when all phonon modes are included, while the labels "modes 1-6" denote the results when only a particular phonon mode is included. The phonon modes are numbered in ascending order of their energies. The label "SR" concerns the results where only short-ranged part of electron-phonon coupling is included. The label "Fröhlich" denotes the results where only mode 6 is included and where Fröhlich model for electron-phonon coupling is used. The label "Fröhlich parab." refers to the previous case where the band energies are replaced with those obtained from a parabolic band dispersion model.

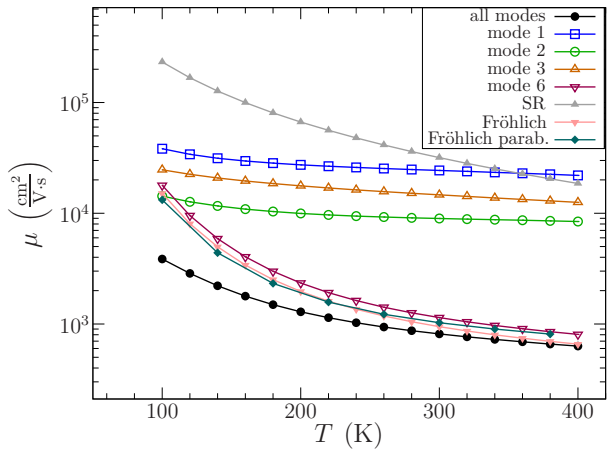

FIG. 37. Temperature dependence of mobility in ZnTe: different contributions and the results from different models. The label "all modes" denotes the results when all phonon modes are included, while the labels "modes 1-6" denote the results when only a particular phonon mode is included. The phonon modes are numbered in ascending order of their energies. The label "SR" concerns the results where only short-ranged part of electron-phonon coupling is included. The label "Fröhlich" denotes the results where only mode 6 is included and where Fröhlich model for electron-phonon coupling is used. The label "Fröhlich parab." refers to the previous case where the band energies are replaced with those obtained from a parabolic band dispersion model.

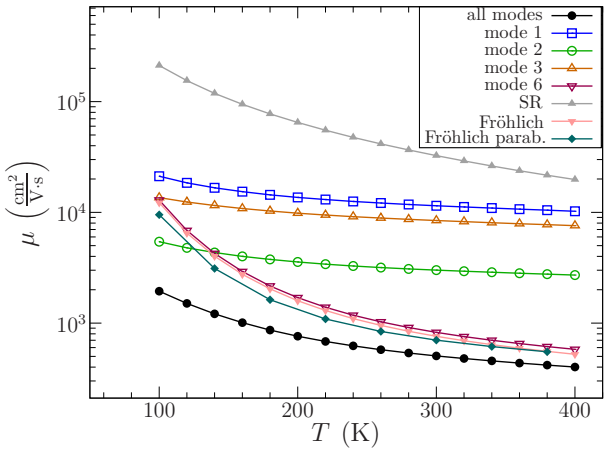

FIG. 38. Temperature dependence of mobility in CdSe: different contributions and the results from different models. The label "all modes" denotes the results when all phonon modes are included, while the labels "modes 1-6" denote the results when only a particular phonon mode is included. The phonon modes are numbered in ascending order of their energies. The label "SR" concerns the results where only short-ranged part of electron-phonon coupling is included. The label "Fröhlich" denotes the results where only mode 6 is included and where Fröhlich model for electron-phonon coupling is used. The label "Fröhlich parab." refers to the previous case where the band energies are replaced with those obtained from a parabolic band dispersion model.

XV. COMPARISON OF ELECTRON-LO-PHONON COUPLING CONSTANTS IN DIFFERENT MODELS

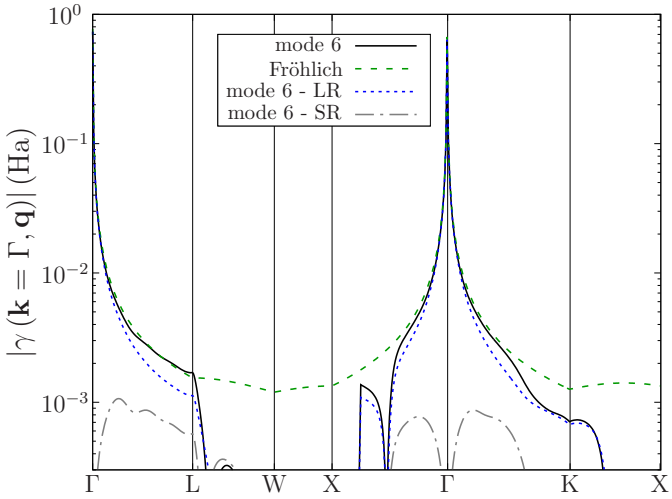

FIG. 39. Electron-phonon coupling constants for scattering of an electron at wave vector $\mathbf{k} = \Gamma$ with a mode 6 phonon at wave vector $\mathbf{q}$ in CdTe. The label "mode 6" denotes the results of the full calculation, "mode 6 - LR" and "mode 6 - SR" denote its long-ranged and short-ranged part, while the label "Fröhlich" denotes the result for the Froöhlich model.

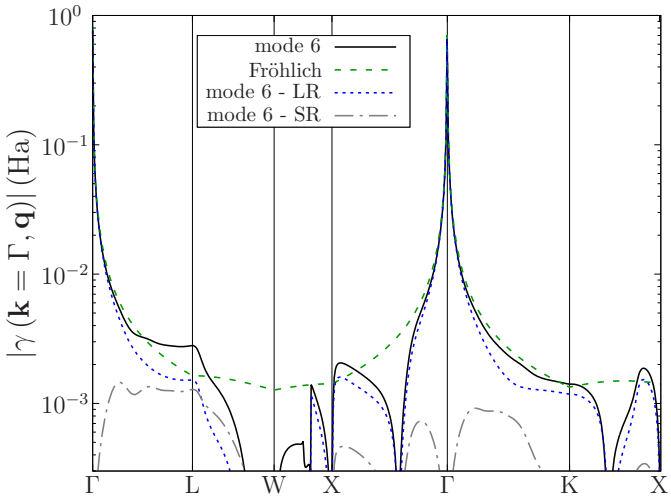

FIG. 40. Electron-phonon coupling constants for scattering of an electron at wave vector $\mathbf{k} = \Gamma$ with a mode 6 phonon at wave vector $\mathbf{q}$ in ZnTe. The label "mode 6" denotes the results of the full calculation, "mode 6 - LR" and "mode 6 - SR" denote its long-ranged and short-ranged part, while the label "Fröhlich" denotes the result for the Froöhlich model.

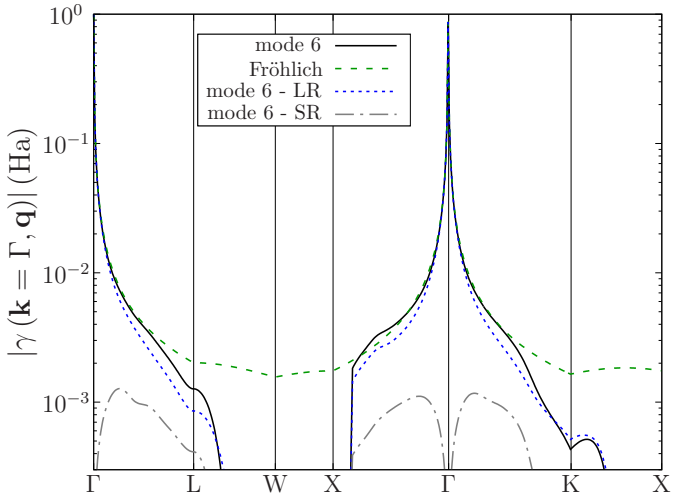

FIG. 41. Electron-phonon coupling constants for scattering of an electron at wave vector $\mathbf{k} = \Gamma$ with a mode 6 phonon at wave vector $\mathbf{q}$ in CdSe. The label "mode 6" denotes the results of the full calculation, "mode 6 - LR" and "mode 6 - SR" denote its long-ranged and short-ranged part, while the label "Fröhlich" denotes the result for the Froöhlich model.

XVI. DEPENDENCE OF MOMENUTUM RELAXATION TIME ON ELECTRONIC ENERGY

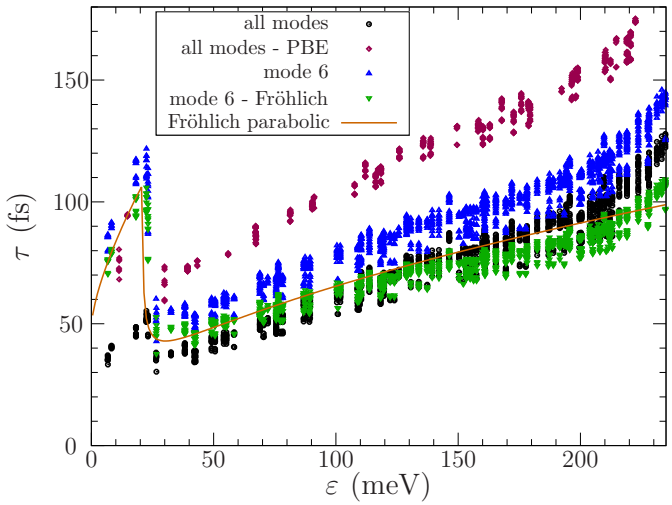

FIG. 42. Dependence of momentum relaxation time on electron energy at a temperature of $T = 300$ K in CdTe. The label "all modes" denotes the results of the full calculation, the label "all modes - PBE" refers to the results of the full calculation when PBE functional is used, the label "mode 6" denotes the results when only phonon mode 6 is included, the label "mode 6 - Fröhlich" denotes the results for the Fröhlich model for mode 6, while the label "Fröhlich parabolic" denotes the results for the Fröhlich model with parabolic band structure.

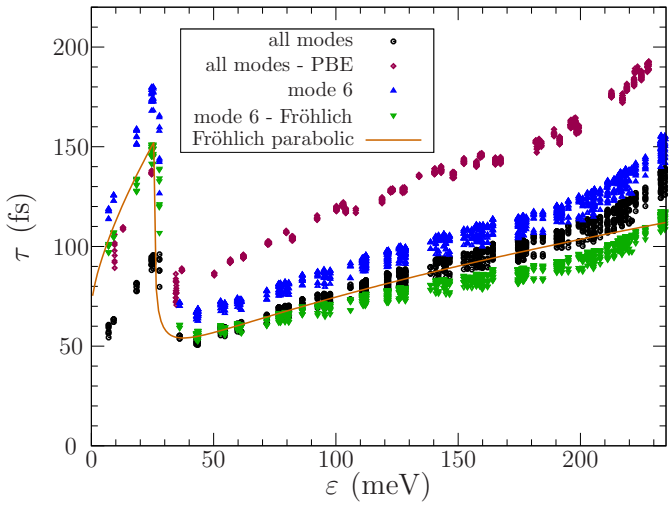

FIG. 43. Dependence of momentum relaxation time on electron energy at a temperature of $T = 300$ K in ZnTe. The label "all modes" denotes the results of the full calculation, the label "all modes - PBE" refers to the results of the full calculation when PBE functional is used, the label "mode 6" denotes the results when only phonon mode 6 is included, the label "mode 6 - Fröhlich" denotes the results for the Fröhlich model for mode 6, while the label "Fröhlich parabolic" denotes the results for the Fröhlich model with parabolic band structure.

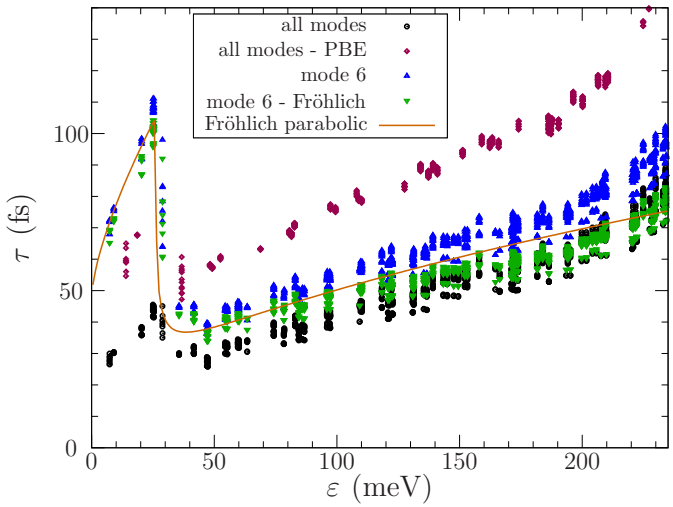

FIG. 44. Dependence of momentum relaxation time on electron energy at a temperature of $T = 300\,\mathrm{K}$ in CdSe. The label "all modes" denotes the results of the full calculation, the label "all modes - PBE" refers to the results of the full calculation when PBE functional is used, the label "mode 6" denotes the results when only phonon mode 6 is included, while the label "mode 6 - Fröhlich" denotes the results for the Fröhlich model for mode 6, while the label "Fröhlich parabolic" denotes the results for the Fröhlich model with parabolic band structure.

XVII. ANALYTIC EXPRESSION FOR MOMENTUM RELAXATION TIME AND SCATTERING TIME IN THE CASE OF FRÖHLICH MODEL WITH PARABOLIC BAND STRUCTURE

In the case of parabolic band structure with effective mass m the momentum relaxation time of an electron at momentum k that interacts with dispersionless phonon mode of energy $\hbar\omega_{\mathrm{LO}}$ via the Fröhlich interaction reads

$$\tau = \frac{1}{W_a + W_e}, \tag{22}$$

where the term

$$W_a = \frac{1}{2\pi}\frac{n_{\mathrm{LO}} mC}{\hbar^3 k}\left[1 - \ln\left|\frac{k+\sqrt{C_1}}{k-\sqrt{C_1}}\right| \cdot \frac{\left(k-\sqrt{C_1}\right)^2}{2k\sqrt{C_1}}\right] \tag{23}$$

comes from phonon absorption and

$$W_e = \frac{1}{2\pi}\frac{\left(n_{\mathrm{LO}}+1\right) mC}{\hbar^3 k}\left[1 - \ln\left|\frac{k+\sqrt{C_2}}{k-\sqrt{C_2}}\right| \cdot \frac{\left(k-\sqrt{C_2}\right)^2}{2k\sqrt{C_2}}\right] \tag{24}$$

comes from phonon emission. In previous equations $n_{\mathrm{LO}} = \frac{1}{e^{\frac{\hbar\omega_{\mathrm{LO}}}{k_B T}} - 1}$ is the number of phonons of energy $\hbar\omega_{\mathrm{LO}}$, $C_1 = k^2 + \frac{2m\omega_{\mathrm{LO}}}{\hbar}$, $C_2 = k^2 - \frac{2m\omega_{\mathrm{LO}}}{\hbar}$ and $C = \frac{\hbar e_0^2 \omega_{\mathrm{LO}}}{2\varepsilon_0}\left(\frac{1}{\varepsilon_r^{\infty}} - \frac{1}{\varepsilon_r^{\mathrm{st}}}\right)$. The phonon emission term should be set to zero when $C_2 < 0$.

The scattering time which is given by Eq. (2) of the paper without the $\cos\theta$ term reads

$$\tau^{\mathrm{sc}} = \frac{1}{W_a^{\mathrm{sc}} + W_e^{\mathrm{sc}}}, \tag{25}$$

where

$$W_a^{\mathrm{sc}} = \frac{1}{2\pi}\frac{n_{\mathrm{LO}} mC}{\hbar^3 k}\ln\left|\frac{k+\sqrt{C_1}}{k-\sqrt{C_1}}\right| \tag{26}$$

and

$$W_e^{\mathrm{sc}} = \frac{1}{2\pi}\frac{\left(n_{\mathrm{LO}}+1\right) mC}{\hbar^3 k}\ln\left|\frac{k+\sqrt{C_2}}{k-\sqrt{C_2}}\right|. \tag{27}$$

XVIII. DEPENDENCE OF MOMENUTUM RELAXATION TIME ON ELECTRONIC ENERGY IN WIDER ENERGY RANGE

The results shown in Fig. 10 of the paper and in Figs. 42-44 indicate that momentum relaxation times follow nicely the prediction of the Fröhlich model in the energy range from one LO phonon energy up to at least 250 meV. It is certainly expected that this agreement will no longer be good at energies that are sufficiently high. To establish at what energies will this happen, we calculated the momentum relaxation times and scattering times for energies up to 1.5 eV above the bottom of the conduction band in the case of ZnSe. The results shown in Fig. 45 indicate that the Fröhlich model with parabolic band structure gives a good description of momentum relaxation times and scattering times for energies up to ~ 600 meV.

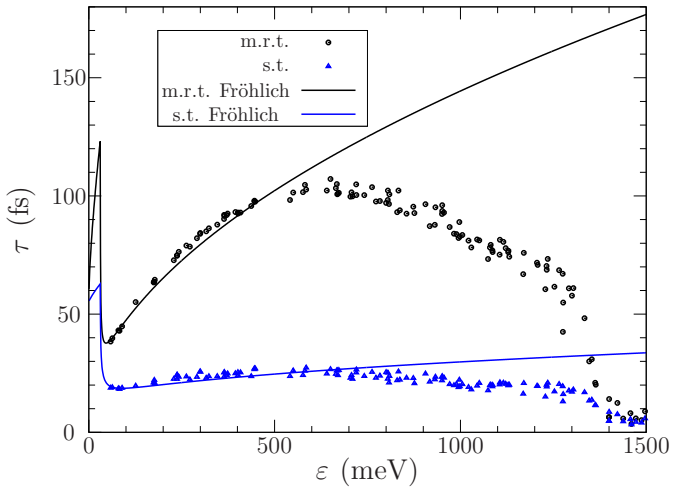

FIG. 45. Dependence of momentum relaxation time (m.r.t.) and scattering time (s.t.) on electron energy at a temperature of $T = 300$ K in ZnSe. The results are shown for electronic states that are randomly selected in such a way that there is on average 1 state per 10 meV. The results obtained from the Fröhlich model with parabolic band structure are shown as full lines.

Next, we compare our results with the results of Refs. [7] (GaN) and [8] (GaAs). It was shown in these references that at low energies scattering rates are almost independent of electron energy. Our results for scattering times in ZnSe are in agreement with these results, while we note that momentum relaxation times do not follow the same trend. At higher energies scattering rates in Refs. [7] and [8] increase (and therefore scattering times decrease). As can be seen in Fig. 45 we also obtain that scattering times decrease at energies above ~ 600 meV. Our results for ZnSe therefore qualitatively follow the same trend as the results for GaN and GaAs. Quantitatively, the Fröhlich model is applicable in ZnSe up to larger energies and scattering times start to decrease at larger energies in ZnSe in comparison to GaN and GaAs.

[1] N. Marzari and D. Vanderbilt, Maximally localized generalized Wannier functions for composite energy bands, Phys. Rev. B **56**, 12847 (1997).
[2] C. Verdi and F. Giustino, Fröhlich electron-phonon vertex from first principles, Phys. Rev. Lett. **115**, 176401 (2015).
[3] G. Brunin, H. P. C. Miranda, M. Giantomassi, M. Royo, M. Stengel, M. J. Verstraete, X. Gonze, G.-M. Rignanese, and G. Hautier, Electron-phonon beyond Fröhlich: Dynamical quadrupoles in polar and covalent solids, Phys. Rev. Lett. **125**, 136601 (2020).
[4] V. A. Jhalani, J.-J. Zhou, J. Park, C. E. Dreyer, and M. Bernardi, Piezoelectric electron-phonon interaction from ab initio dynamical quadrupoles: Impact on charge transport in wurtzite GaN, Phys. Rev. Lett. **125**, 136602 (2020).
[5] J. Sjakste, N. Vast, M. Calandra, and F. Mauri, Wannier interpolation of the electron-phonon matrix elements in polar semiconductors: Polar-optical coupling in GaAs, Phys. Rev. B **92**, 054307 (2015).
[6] S. Adachi, *Handbook on Physical Properties of Semiconductors, Volume 3, II-VI Compound Semiconductors* (Kluwer Academic Publishers, Boston, 2004).
[7] V. A. Jhalani, J.-J. Zhou, and M. Bernardi, Ultrafast hot carrier dynamics in GaN and its impact on the efficiency droop, Nano Lett. **17**, 5012 (2017).
[8] J.-J. Zhou and M. Bernardi, Ab initio electron mobility and polar phonon scattering in GaAs, Phys. Rev. B **94**, 201201 (2016).